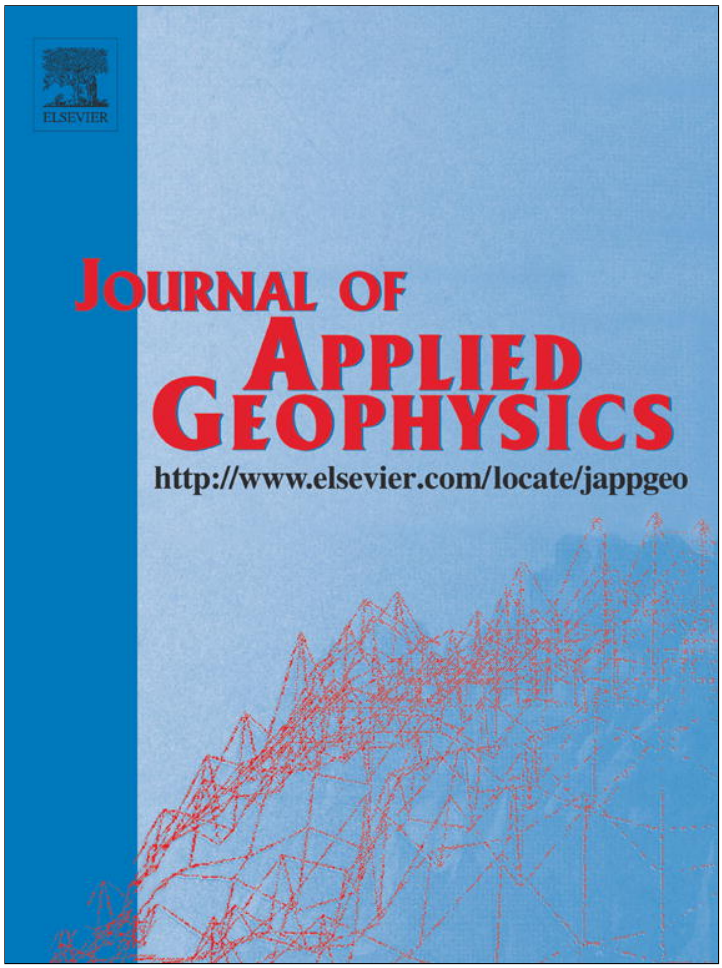

(This is a sample cover image for this issue. The actual cover is not yet available at this time.)

Journal of Applied Geophysics 89 (2013) 48–67

Contents lists available at SciVerse ScienceDirect

Journal of Applied Geophysics

journal homepage: www.elsevier.com/locate/jappgeo

Detection and extraction of orientation-and-scale-dependent information from two-dimensional GPR data with tuneable directional wavelet filters

Andreas Tzanis *

Department of Geophysics and Geothermy, National and Kapodistrian University of Athens, Panepistimiopoli, Zografou 15784, Greece

ARTICLE INFO

Article history:
Received 29 July 2012
Accepted 12 November 2012
Available online 23 November 2012

Keywords:
GPR data
B-spline wavelets
Gabor filter
Directional filter
Multi-scale analysis
Denoising

ABSTRACT

The Ground Probing Radar (GPR) is a valuable tool for near surface geological, geotechnical, engineering, environmental, archaeological and other work. GPR images of the subsurface frequently contain geometric information (constant or variable-dip reflections) from various structures such as bedding, cracks, fractures, etc. Such features are frequently the target of the survey; however, they are usually not good reflectors and they are highly localized in time and in space. Their scale is therefore a factor significantly affecting their detectability. At the same time, the GPR method is very sensitive to broadband noise from buried small objects, electromagnetic anthropogenic activity and systemic factors, which frequently blurs the reflections from such targets.

This paper introduces a method to de-noise GPR data and extract geometric information from scale-and-dip dependent structural features, based on one-dimensional B-Spline Wavelets, two-dimensional directional B-Spline Wavelet (BSW) Filters and two-dimensional Gabor Filters. A directional BSW Filter is built by sidewise arranging s identical one-dimensional wavelets of length L, tapering the s-parallel direction (span) with a suitable window function and rotating the resulting matrix to the desired orientation. The length L of the wavelet defines the temporal and spatial scale to be isolated and the span determines the length over which to smooth (spatial resolution). The Gabor Filter is generated by multiplying an elliptical Gaussian by a complex plane wave; at any orientation the temporal or spatial scale(s) to be isolated are determined by the wavelength. λ of the plane wave and the spatial resolution by the spatial aspect ratio γ, which specifies the ellipticity of the support of the Gabor function. At any orientation, both types of filter may be tuned at any frequency or spatial wavenumber by varying the length or the wavelength respectively. The filters can be applied directly to two-dimensional radargrams, in which case they abstract information about given scales at given orientations. Alternatively, they can be rotated to different orientations under adaptive control, so that they remain tuned at a given frequency or wavenumber and the resulting images can be stacked in the LS sense, so as to obtain a complete representation of the input data at a given temporal or spatial scale. In addition to isolating geometrical information for further scrutiny, the proposed filtering methods can be used to enhance the S/N ratio in a manner particularly suitable for GPR data, because the frequency response of the filters mimics the frequency characteristics of the source wavelet. Finally, signal attenuation and temporal localization are closely associated: low attenuation interfaces tend to produce reflections rich in high frequencies and fine-scale localization as a function of time. Conversely, high attenuation interfaces will produce reflections rich in low frequencies and broad localization. Accordingly, the temporal localization characteristics of the filters may be exploited to investigate the characteristics of signal propagation (hence material properties). The method is shown to be very effective in extracting fine to coarse scale information from noisy data and is demonstrated with applications to noisy GPR data from archaeometric and geotechnical surveys.

1. Introduction

The purpose of this paper is to investigate methods of S/N enhancement and information retrieval from Ground Probing Radar (GPR) data, with particular emphasis placed on the problem of recovering features associated with specific temporal or spatial scales and geometry (orientation/dip). The Ground Probing Radar (GPR) has become a valuable, almost indispensable means of exploring thin and shallow structures for geological, geotechnical, engineering, environmental, archaeological and other work. GPR images frequently contain geometric (orientation/dip-dependent) information from point scatterers (e.g. diffraction hyperbolae), dipping reflectors (geological bedding, structural interfaces, cracks, fractures, joints) and other conceivable structural configurations.

* Tel.: +30 2107274785.
E-mail address: atzanis@geol.uoa.gr.

0926-9851/$ – see front matter © 2012 Published by Elsevier B.V.
http://dx.doi.org/10.1016/j.jappgeo.2012.11.007

In geological, geotechnical and engineering applications, this information is valuable and frequently the target of the GPR survey.

At the same time, the GPR method is notoriously susceptible to noise. For example, boulders, animal burrows, tree roots, and other small scale objects and structures can cause unwanted reflections or scattering. Analogous interference is produced by anthropogenic structures and can include reflections from nearby vehicles, buildings, fences, power lines, and trees. Electromagnetic transmissions from cellular telephones, two-way radios, television, and radio and microwave transmitters may also cause noise on GPR records. These types of reflections are only partially countered with shielded antennae while the interference by extraneous or reflected airwaves, critically refracted airwaves and groundwaves cannot be easily suppressed during acquisition. Finally, there is systemic noise, frequently manifested in the form of ringing. Because the GPR source wavelet is tuned at a single operating frequency, the information returned by the subsurface structure is usually limited to a relatively narrow band around it (plus a tail due to dispersion) and, quite frequently, the rest of the spectrum is swamped in noise. Raw GPR data require post-acquisition processing, as they usually provide only approximate target shapes and distances (depths).

Wavelet-based processing and analysis methods have been extensively applied to images (extraction of information, compression and de-noising). Two-dimensional geophysical data, either in the form of potential field anomaly maps, seismic sections, GPR sections, etc., are very similar to an image if each data point is taken to be a pixel. As a consequence, the same wavelet-based methods have been quite extensively adapted to the processing of seismic and potential-field geophysical data. However, they have quite rarely been applied to GPR data.

The wavelet-based method commonly used for the treatment of geophysical data is Multi-Resolution Analysis (MRA, see Chui, 1992; Mallat, 1999). This is the design method of most of the practically relevant discrete wavelet transforms and the justification of the fast wavelet transform; it is commonly applied for image compression (e.g. Stollnitz et al., 1995) and de-noising (e.g. Mohideen et al., 2008). MRA allows a space $L^2(\mathbb{R})$ (image) to be decomposed into a sequence of nested subspaces (images) $L^2(\mathbb{R})\supset\ldots\supset V_n\supset\ldots\supset V_0\supset\ldots\{0\}$, arranged in order of increasing detail (scale), that satisfies certain self-similarity relations in time/space and scale/frequency, as well as completeness and regularity relations. This way, the MRA provides an efficient tool to suppress events of specific scales locally but leave the rest of the data unaffected. The MRA has been introduced to the processing of reflection seismics fairly recently, with most of the related studies attempting to develop efficient noise suppression procedures in a time-frequency sense. Inasmuch as the GPR method is effectively equivalent to reflection seismics, GPR data can be processed with similar techniques. The pertinent literature (seismic and GPR) is not rich, but is steadily growing in numbers and applications (e.g. Deighan and Watts, 1997; Jeng et al., 2009; Leblanc et al., 1998; Matos and Osorio, 2002; Miao and Cheadle, 1998; Nuzzo and Quarta, 2004).

MRA, as applied in the literature quoted above, is not suitable for processing orientation-dependent data. This problem has been addressed by advanced MRA-like algorithms such as the Ridgelet Transform (Candès, 1999; Candès and Donoho, 1999) and the second generation Curvelet Transform (Candès and Donoho, 2003a, 2003b); these will be the subject of a follow-up investigation and will not be examined herein. One may also mention a host of similar "X-let transforms", such as wedgelets (Donoho, 1999), beamlets (Donoho and Huo, 2002), bandlets (Mallat and Peyré, 2007), contourlets (Do and Vetterli, 2005), wave atoms (Demanet and Ying, 2007), surfacelets (Lu and Do, 2007) and others that are certain to have escaped the Author's attention. All these have been proposed independently to identify and restore geometric features.

All these algorithms are pyramidal type decompositions in which the self-similarity relations in time/space and frequency/scale comprise a small number of scaling steps, usually arranged in powers of 2. This allows for a computationally compact decomposition, but is somewhat "inefficient" if one wishes to look into particular temporal or spatial scales. Increasing the order of the decomposition may not always be feasible or effective and may introduce cumbersome redundancy. Moreover, pyramidal decompositions may not always be suitable for GPR data because the source wavelet is tuned at a single operating frequency and, although the signal spreads as it propagates, the information returned by the subsurface structure is usually limited to a relatively narrow band around the nominal frequency. As a consequence, the GPR signal often contains a lot of redundant information (including noise), which may introduce analogous redundancy in the decomposition.

If one wishes to study specific scales and geometrical characteristics (orientations), an alternative approach is to implement Directional Filters (Directional Wavelets). These are useful in many image processing tasks such as texture analysis, edge detection, image and data compression, motion analysis, and image enhancement. Steerable Wavelets are an early form of Directional Filters (Freeman and Adelson, 1991; Simoncelli et al., 1992) and are closely related to the Gabor wavelets (e.g. Feichtinger and Strohmer, 1998, 2003; Lee, 2008). In comparison to separable orthonormal wavelets, the Steerable Wavelets provide translation-invariant and rotation-invariant representations of the position and the orientation of image structures at the expense of high redundancy. Gabor wavelets have mainly been applied to image classification and texture analysis. The main differences between the "early methods" (Steerable Wavelets, Gabor wavelets, etc.) and other "advanced" X-lets is that the early methods do not allow for a different number of directions at each scale; in order to acquire a complete representation of all directions at each scale, it is often required to apply the same filter rotated to different angles under adaptive control and combine the filter outputs.

Finally, it is worth noting that almost all of the methods reviewed above have been developed for application to images, i.e. functions in which the independent variables are of the same nature (spatial) and have identical or comparable sampling rates. In this case, the application of the same filter (wavelet, X-let, etc.) at different orientations has no effect on scale. On the other hand, GPR (or seismic) data are functions in which the independent variables are of different nature (time vs. space) and have incomparable sampling rates. In consequence, as also will be shown later on, the straightforward application of the same filter at different orientations may cause unwanted mixing of different temporal and spatial scales. This is a rather unappreciated factor and (occasionally) may result in poor localization of distinct temporal or spatial data features.

To summarize, there are two lines of approach in analyzing scale-and-orientation dependent data: a) to implement orientation-sensitive MRA type analysis, which may not always be efficient at targeting specific scales, and, b) to use directional filters which may generate redundancy but are tuneable at specific (temporal/spatial) scale-and-orientation dependent features. This work follows the second approach, while trying to devise techniques to reduce redundancy, avoid mixing of different temporal and spatial scales and maintain simplicity of design and operation. To this effect, it will introduce a set of directional filters based on 2-D semi-orthogonal wavelet arrays and evaluate a set of 2-D orthogonal wavelets, both of which can be manipulated to select specific frequencies/scales at any orientation. The former set is based on B-Spline wavelet filters and the latter on the well known Gabor Filter. At a given orientation, both these filters are shown to be highly adaptive and efficient. For instance, it will be shown that it is possible to discriminate between reflections from constant dip — small aperture cracks as opposed and reflections from constant dip (larger) fractures. Moreover, a method will be demonstrated, by which to combine the same frequency or scale selected at different orientations, so as to recover a complete representation of the input data at a single, orientation-independent frequency or scale (for instance, variable dip — small aperture cracks vs. variable dip — fractures).

2. One-dimensional B-Spline Wavelet Filters

The wavelet transform can decompose a spatial or temporal data series into a spectrum of energy levels at given wavelength bands and given locations. In effect, the wavelet transform matches the spatial or temporal localization of the data to the wavelength of interest, providing fine resolution at short wavelengths and broad localization at long wavelengths. This is much more versatile and informative than the Fourier transform, which will provide the power spectrum at given wavelength bands but for the *entire* data series, smoothing out any wavelength-local characteristics. On a single scale the wavelet transform is based on a linear, narrow-band filter. For multi-scale analysis the wavelet can be rescaled to longer and shorter lengths, providing a suite of different size filters, which are convolved with the data to pick out features with wavelengths matching the filters' bandwidths: small-scale events will match small wavelets but not large wavelets and vice versa. By applying the suite of filters it is possible to identify local spatio-temporal characteristics, as well as to distinguish features on different scales (or even identify regions where events of certain scales are missing).

The filters discussed herein are based on B-Spline wavelets, constructed by a shifting, weighting and summing of the B-Spline functions $N_m(x)$, where x is a temporal or spatial variable and m is the order of the spline (B-Spline is shorthand for Basis Spline). Details on B-Splines and the construction of B-Spline wavelets can be found in Chui (1992), Daubechies (1992), Ueda and Lodha (1995) and others, while Unser (1997) argues the case for using B-Spline wavelets. Consequently, only basic information will be given here.

Typically, the m-th order B-Spline is defined recursively by convolution:

$$N_1(x)=\begin{cases}0 & x<0\\ 1 & 0\le x<1\\ 0 & x\ge 1\end{cases},\quad N_m(x)=\int_{-\infty}^{\infty}N_{m-1}N_1(t)dt=\int_0^1 N_{m-1}(x-t)dt.$$

It is apparent that $N_m(x)>0$ for $0<x<m$ and that the 1st order B-Spline $N_1(x)$ is the Haar scaling function. The two-scale relation for B-Spline scaling functions of general order m is written as

$$N_m(x)=\sum_{k=0}^{m}p_k N_m(2x-1)=\sum_{k=0}^{m}2^{-m+1}\binom{m}{k}N_m(2x-1),\quad 0\le k<m.$$

where p_k is the two-scale sequence. The B-Splines have compact support in the interval $[0, m]$ and they are symmetric with respect to $m/2$ for every $x\in\Re$. Finally, $\sum_{k=-\infty}^{\infty}N_m(x-k)=1$, meaning that they have partition of unity.

Since B-Splines N_m are scaling functions, they can be associated with wavelets β_m: the two-scale relation for B-Spline wavelets of general order m is given by

$$\beta_m(x)=\sum_{k=0}^{3m-2}q_k N_m(2x-k),\quad q_k=(-1)^k 2^{1-m}\sum_{l=0}^{m}\binom{m}{l}N_{2m}(k+1-l) \tag{1}$$

where q_k comprise finite series (only $3\,m-1$ terms are non-zero). The support of β_m is $[0,\ 2\,m-1]$ for $m=1,\ 2,\ \ldots$ and is *compact*; they are symmetric for even m, i.e. $\beta_m(x)=\beta_m(2m-1-x)\ \forall m=2j$, anti-symmetric for odd m, i.e. $\beta_m(x)=-\beta_m(2m-1-x)\,\forall m=2j+1$ and exhibit complete oscillation property. Moreover, they have vanishing moments ($\int_{-\infty}^{\infty}\beta_m(x)x^i dx=0,\ i=0,1,\ \ldots\ m-1$) and are orthogonal at different scales, that is $\left[\beta_m\left(2^{j_1}x-k_1\right),\beta_m\left(2^{j_2}x-k_2\right)\right]=0$ if $j_1\neq j_2$, although different translates of the same wavelet are not orthogonal at the same scale, that is $[\beta_m(2^j x-k_1),\ \beta_m(2^j x-k_2)]\neq 0$ if $m\neq 1$; this property is referred to as *semi-orthogonality*.

B-Spline wavelets (i.e. the wavelet coefficients) can be constructed directly from (1), but the result may not always have the desirable spectral properties. For instance, the cubic B-Spline wavelet $\beta_4(x)$ calculated by Ueda and Lodha (1995) turns out with a non-trivial dc component and exhibits a significant phase shift at the lower frequency range and phase instability at higher frequencies and large scales. In consequence, and after due consideration of their spectral characteristics, the numerical realizations of the B-Spline wavelets to be used in this study were chosen as follows:

For the linear and quadratic wavelets, the direct construction based on the two-scale B-Spline function and Eq. (1) turned out to be the optimal alternative. Thus, the *linear* B-Spline wavelet is

$$\beta_2(x)=\frac{1}{12}[N_2(2x)-6N_2(2x-1)+10N_2(2x-2)-6N_2(2x-3)+N_2(2x-4)]$$

and the quadratic wavelet is

$$\beta_3(x)=\frac{1}{480}[N_3(2x)-29N_3(2x-1)+147N_3(2x-2)-303N_3(2x-3)$$
$$+303N_3(2x-4)-147N_3(2x-5)+29N_3(2x-6)-N_3(2x-7)]$$

These are also the realizations proposed by Ueda and Lodha (1995).

For the cubic B-Spline wavelet $\beta_4(x)$, the realization of Katunin and Korczak (2009) was adopted. These authors construct an elaborate piecewise approximation of the wavelet with cubic polynomials over short intervals of its support. The analytic form of the approximation is lengthy and is not presented herein for the sake of brevity, but it turns out to comprise a consistent function with stable and smooth spectral characteristics. Finally, the derivative of the cubic B-Spline $N_4(x)$ also comprises a wavelet (Canny, 1986). It can be computed analytically, directly from $N_2(x)$.

B-Spline wavelet filters comprise a family with a broad spectrum of frequency localization properties. The top panel of Fig. 1 shows the frequency responses of the B-Spline wavelet family when tuned at the nominal frequency of 400 MHz, for data recorded with a sampling rate of 0.1957 ns. The bottom panel of Fig. 1 is the same but for a tuning frequency of 100 MHz and a sampling rate of 0.7828 ns. The tuning of the different filters at the same frequency is achieved by adjusting (expanding or contracting) their lengths. The shape of the frequency responses asserts that different order filters extract different information. The Cubic B-Spline Derivative allows quite a broad spectral band around the tuning frequency, while the Linear, Quadratic and Cubic B-Splines pass progressively narrower bands, thus facilitating progressively finer frequency localization and temporal scale extraction. Moreover, the frequency responses are all shaped like slightly asymmetric bells; in this capacity they *mimic*, more or less, the shape of the radar source wavelet. Based on this property, it may be argued that this type of filter is particularly suitable (adaptive) for GPR data. Notably, the Ricker (or Mexican Hat) wavelet, one of the commonly implemented models of the radar source pulse, can also be approximated by derivatives of Cardinal B-Splines (Brinks, 2008).

2.1. GPR data Analysis with One-dimensional B-Spline Wavelet Filters

A number of examples will now be presented, in order to demonstrate how these wavelets operate on GPR data and provide a measure of the information to be mined with this approach. The wavelets will be applied, first to individual traces (also known as A-scans) for a detailed study of their performance and, then, to complete two-dimensional radargrams (also known as B-scans).

The first example is a trace from an archaeometric survey at the ancient Agora (Forum) of Argos, Greece, in an attempt to locate the temple of Apollo Lyceus. The 16-bit data was collected in B-scan mode with a GSSI SIR-2000 system and 400 MHz antenna. The trace shown in Fig. 2a contains strong reflections from buried targets (man-made structures) in the two-way traveltime interval 18–30 ns and weak reflections buried in heavy noise in the interval 60–80 ns.

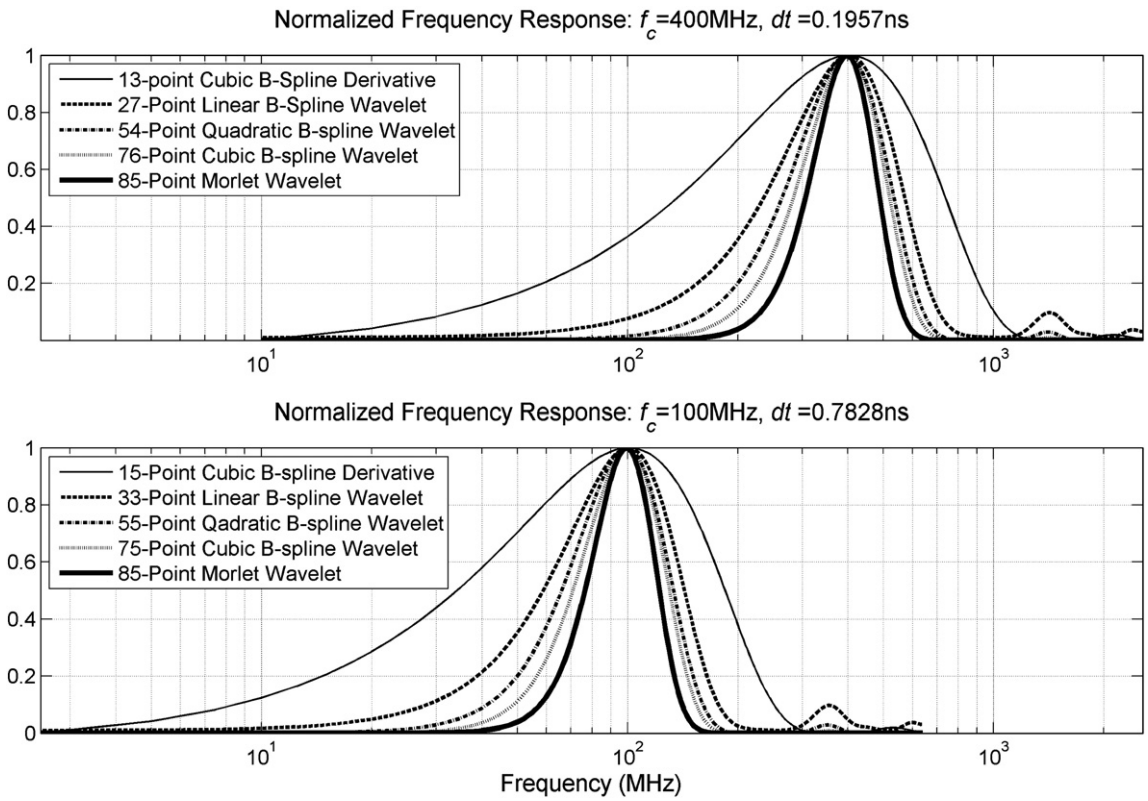

Fig. 1. Normalized frequency responses of the B-Spline wavelet family, assuming a nominal central frequency of 400 MHz for data recorded with a sampling rate of 0.1957 ns (top) and a nominal central frequency/sampling rate of 100 MHz/0.7828 ns respectively (bottom). The corresponding frequency response of the well known Morlet wavelet is also shown for reference.

The data is also contaminated by long period noise which appears *after* 30 ns and short period noise localized between 40 and 50 ns (low amplitude) and 60–80 ns (high amplitudes). However, the most distressing and possibly misleading characteristic of the noise is a series of reverberations spread between 100 and 200 MHz and exhibiting three spectral peaks at 110 MHz, 140 MHz and 170 MHz; this is clearly a structured process of uncertain origin, possibly antenna self-clutter, with power comparable to the power content of the data (if the data is assumed to be spread mainly in the interval 200–600 MHz). An expression of this noise can be seen quite clearly between 30 and 50 ns, but at later times it fuses with the data and other noise processes, so that its amplitude and temporal extent cannot be certain.

This trace is treated with a *cubic B-Spline derivative* wavelet. Fig. 2b shows the output of a 5-point wavelet; the frequency response of this filter peaks at ~1.28 GHz and is tuned with data features having temporal scales of the order of 0.6–1.6 ns. This is actually the scale of the short period noise; therefore, the output of the filter is effectively a representation (model) of the short-period noise, although some attenuated data components also appear to leak into the output series around the 18–30 ns interval. Fig. 2c shows the output of a 110-point wavelet with frequency response tuned at ~0.06 MHz; these are the longest periods in the input data series and correspond to the temporal scales of long period noise: the output of the filter is effectively a model of the long period noise. Fig. 2d shows the output of a 42-point wavelet tuned at 140 MHz and processes with temporal scales of the order 4–16 ns. The power of the output series is mainly to be found in the frequency interval 60–200 MHz, therefore it comprises a model of the reverberating noise described above. It is now evident that this process has variable amplitude which is significant and comparable to the amplitude of reflections from buried targets, particularly at the early part of the trace; moreover, it maximizes at 30–40 ns and 60–75 ns and practically disappears after the 80th ns. Finally, Fig. 2e shows the output of a 15-point wavelet. The frequency response of this wavelet peaks at ~399 MHz, almost in tune with the nominal central frequency of the antenna and selects data features with temporal scales of the order of 2–5 ns. This is comparable to the duration of the main reflection events and very different from the temporal scale of the noise: this output trace essentially comprises *noise-free* data!

In this example the cubic B-Spline derivative wavelet was almost adequate. However, in the very next scan, only 1 m to the left and 5 minutes later, the distributed 100–200 MHz noise processes have coalesced into a single, powerful and dominant spectral peak at approx. 200 MHz (Fig. 3a). The cubic B-Spline derivative wavelet tuned at 400 MHz cannot suppress this feature due to its broad frequency response (Fig. 3b). In this case it is the *linear B-Spline wavelet* which provides adequate noise suppression (Fig. 3c), while the tuned quadratic and cubic wavelets offer finer frequency localization and scale extraction (Fig. 3d–e). Fig. 4a illustrates the raw (B-scan) radargram whence the trace of Fig. 3 was extracted; Fig. 4b is the same data, after application of a 27-point linear B-Spline wavelet tuned at 400 MHz. The noise comprises sporadic high frequency bursts possibly related to the operation of communication devices (the data was collected in a semi-urban environment), a long period air-wave between 0 and 20 m from a nearby reflector and persistent banding with a peak at approx. 200 MHz, which is attributed to antenna self-clutter. The existence of a peculiar X-shaped noise process at approx. 10 m down the scan line and between 20 and 60 ns is also of interest. The presence of buried, presumably man-made objects is also evident at several locations along the radargram. The filter appears to have effectively removed the noise (Fig. 4b), while some residual banding can be easily eliminated with conventional methods (e.g. subtraction of a global background). The inset

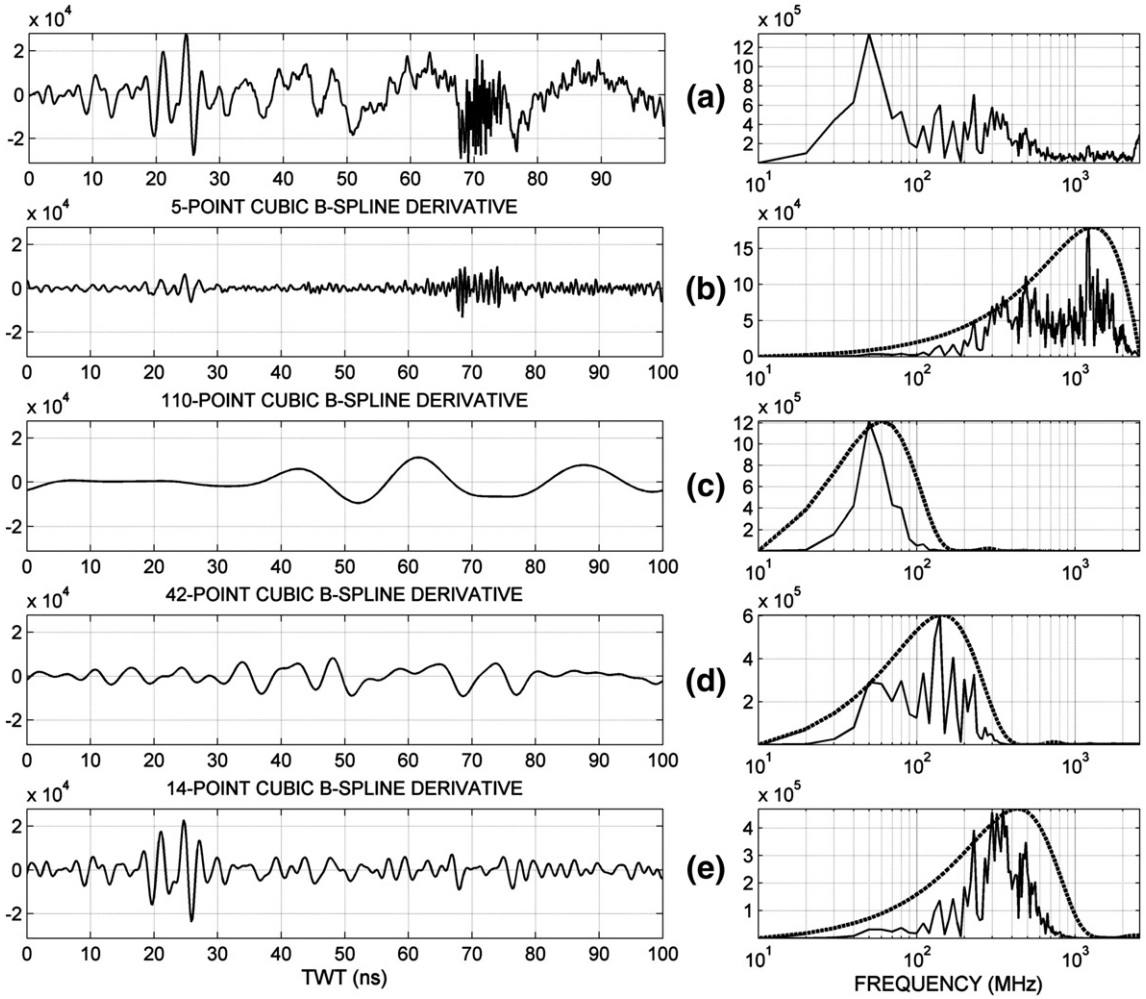

Fig. 2. Application of a *cubic B-spline derivative* wavelet filter to a 16-bit data trace collected with a 400 MHz antenna and contaminated by noise of different temporal scales. The left column shows raw and processed traces; the right column the corresponding frequency responses. **(a)** The raw trace. **(b)** The frequency response of a 5-point filter peaks at approx. 1.28 GHz; the filter essentially yields a model of the short-period noise. (**c**) The response of a 110-point filter peaks at approx. 0.06 MHz; the filter yields a model of the long period noise. (**d)** A 42-point wavelet with peak frequency at 140 MHz recovers a model of noise introduced by antenna self-clutter. **(e)** A 15-point filter has a frequency peaking at approx. 399 MHz and yields a model of the data with minimal contamination.

figure points to steep reflections and diffractions from (presumably) man-made structures that have previously been almost completely obscured by the X-shaped interference.

3. Two-dimensional oriented and tuneable B-spline wavelet filters

When the data depend on two spatial dimensions, (a matrix or image), the wavelet transform decomposes it into a series of images, each of which contains information at a specific location, of features at a single scale. In GPR data, the existence of two independent variables (time/space) allows each component of the *f*–*k* spectrum to be coupled with a particular orientation (dip). Thus, it appears feasible to design a matrix filter in which the temporal/spatial scale and dip can be varied so as to be tuneable at any trait in the data. In such a filter the scale would be determined by the dimensions of the matrix and the dip by the *orientation* of the matrix relative to the time (t) and space (x) axes. It follows that the precision in location (resolution) of any feature in the wavelet transform will depend on its scale. Fig. 5 illustrates how to design such a two-dimensional filter:

1. Generate a one-dimensional wavelet of the desired order and length (e.g. Fig. 5a). The *length* (L) of the wavelet comprises the longitudinal dimension of the matrix filter.
2. Sidewise arrange a number of identical one-dimensional wavelets to create a 2-D matrix. The number of parallel wavelets comprises the transverse dimension of the matrix filter and will henceforth be referred to as the *span* (s) of the filter.
3. Taper the transverse (span-parallel) direction with a smoothing window function (e.g. Gaussian or Hanning window — see Fig. 5b).
4. If the length of the wavelet is parallel to the time axis and the span parallel to the space axis, the resulting filter should have the form of the example in Fig. 5c. It is also possible to design a *transposed* filter with its length parallel to the space axis and its span parallel to the time axis. If $\mathbf{b}(t, x)$ denotes any such matrix filter, note that although the condition $\int_t \int_x \mathbf{b}(t,x)\mathrm{d}x\mathrm{d}t = \int_x \int_t \mathbf{b}(t,x)\mathrm{d}t\mathrm{d}x = 0$ is satisfied, this comprises a departure from strict biorthogonal wavelet construction because the span-parallel direction is not a wavelet!
5. Let the time axis (t) correspond to the direction of 0° and the space axis (x) to the direction of 90°, i.e. let the azimuth be measured clockwise with respect to the time axis. In order to de-noise and/or isolate dipping reflectors rotate the matrix filter to the desired azimuth (*dip direction*), so that the span of the filter will be parallel to the alignment of reflections and the length perpendicular to it (Fig. 5e).

This matrix operator will henceforth be referred to with the acronym *BSW Filter* (for B-Spline Wavelet Filter). It should also be

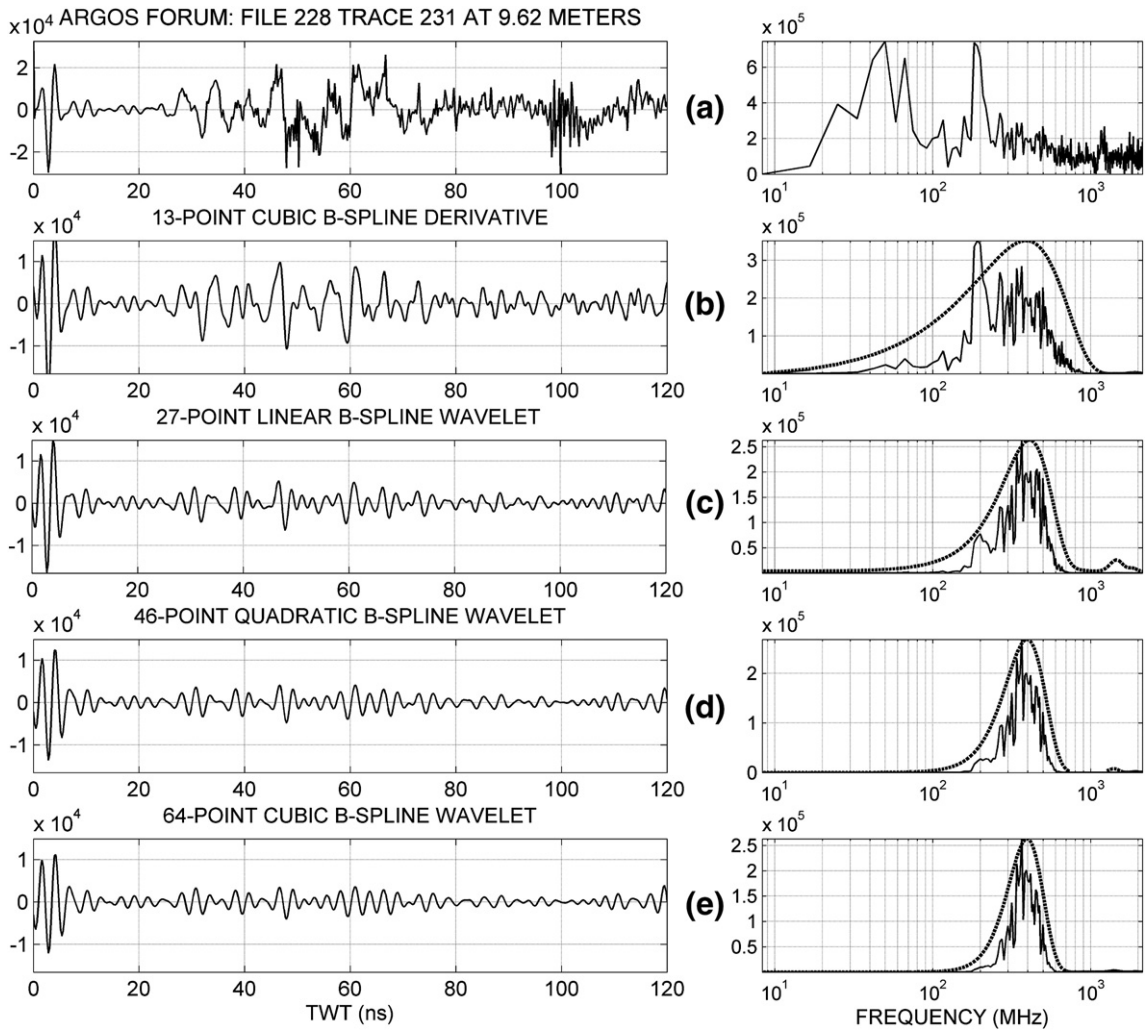

Fig. 3. Application of the B-spline wavelet family to a 16-bit data trace collected with a 400 MHz antenna and contaminated by noise of different temporal scales. **(a)** The principal source of noise is antenna self-clutter with a dominant spectral peak at approx. 200 MHz. **(b)** The cubic B-spline derivative at 400 MHz cannot suppress this feature. **(c)** The linear B-spline wavelet at 400 MHz provides adequate noise suppression. **(d-e)** The quadratic and cubic B-spline wavelets at 400 MHz offer sharper frequency localization and finer-scale extraction.

noted that the concept of the BSW Filter originated with the work of Little et al. (1993) and Little (1994) who applied it to the analysis of topographic and bathymetric data.

The rotation of the BSW Filter should be understood thus: Let there be an operator $\mathbf{R}\{\theta\}$ capable of rotating real functions $\mathbf{b}(t, x)$ of a fixed coordinate system through an angle θ. Then, the operation $\mathbf{R}\{\mathbf{b}(t, x)\colon \theta\}$ creates a new function $\mathbf{b}^{\theta}(t, x)$ which is numerically equal to $\mathbf{b}(t^{\theta}, x^{\theta})$, where the superscript θ indicates that the coordinate system has been rotated by $\mathbf{R}\{\theta\}$ through an angle θ. For instance, the transformation of first column of $\mathbf{b}(t, x)$ would be:

$$\begin{bmatrix} x_1^{\theta} \\ t_1^{\theta} \\ x_1^{\theta} \\ t_2^{\theta} \\ \vdots \\ x_1^{\theta} \\ t_M^{\theta} \end{bmatrix} = \begin{bmatrix} \cos\theta & -\sin\theta & 0 & 0 & \cdots & 0 & 0 \\ \sin\theta & \cos\theta & 0 & 0 & \cdots & 0 & 0 \\ 0 & 0 & \cos\theta & -\sin\theta & \cdots & 0 & 0 \\ 0 & 0 & \sin\theta & \cos\theta & \cdots & 0 & 0 \\ \vdots & \vdots & \vdots & \vdots & \ddots & \vdots & \vdots \\ 0 & 0 & 0 & 0 & \cdots & \cos\theta & -\sin\theta \\ 0 & 0 & 0 & 0 & \cdots & \sin\theta & \cos\theta \end{bmatrix} \cdot \begin{bmatrix} x_1 \\ t_1 \\ x_1 \\ t_2 \\ \vdots \\ x_1 \\ t_M \end{bmatrix}$$

The mapping applied to the m-th element of the first column is $b(t_m,x_1) \leftrightarrow b(t_m^{\theta},x_1^{\theta}) = b^{\theta}(t_m,x_1)$, so that when the transformation is applied to the entire matrix operator $\mathbf{b}(t, x)$, the result will be $\mathbf{b}(t^{\theta}, x^{\theta}) = \mathbf{b}^{\theta}(t,x)$.

At a given angle θ the f–k spectrum of the BSW Filter $\mathbf{b}^{\theta}(t, x)$ will be

$$\mathbf{B}^{\theta}(f,k) = \int_{-\infty}^{\infty}\int_{-\infty}^{\infty} \mathbf{b}^{\theta}(t,x)\cdot e^{-j2\pi kx} e^{-j2\pi ft}\,\mathrm{d}x\mathrm{d}t \tag{2}$$

At the rotated coordinate system the f–k spectrum of $\mathbf{b}(t^{\theta}, x^{\theta})$ will be

$$\mathbf{B}\left(f^{\theta},k^{\theta}\right) = \int_{-\infty}^{\infty}\int_{-\infty}^{\infty} \mathbf{b}\left(t^{\theta},x^{\theta}\right)\cdot e^{-j2\pi k^{\theta}x} e^{-j2\pi f^{\theta}t}\,\mathrm{d}x\mathrm{d}t \tag{3}$$

Because $\mathbf{b}^{\theta}(t,x) = \mathbf{b}(t^{\theta},x^{\theta})$, it is possible to have $\mathbf{B}^{\theta}(f,k) = \mathbf{B}(f^{\theta},k^{\theta})$ only when $f \equiv f^{\theta}$ and $k \equiv k^{\theta}$. This is a heuristic way of showing that the f–k spectrum of the matrix operator rotates *identically* with its t–x counterpart (Fig. 5d, f).

The f–k spectrum consists of two lobes symmetric with respect to the origin. Owing to the scaling properties of the B-Spline wavelets, it is straightforward to verify that the location of the peak with respect to the frequency axis (f^{θ}) and wavenumber axis (k^{θ}), is determined exclusively by the length (scale) of the wavelet which thus defines the temporal and spatial scale(s) to be isolated. The shape of the lobes is determined by the type/order and length of the wavelet, the

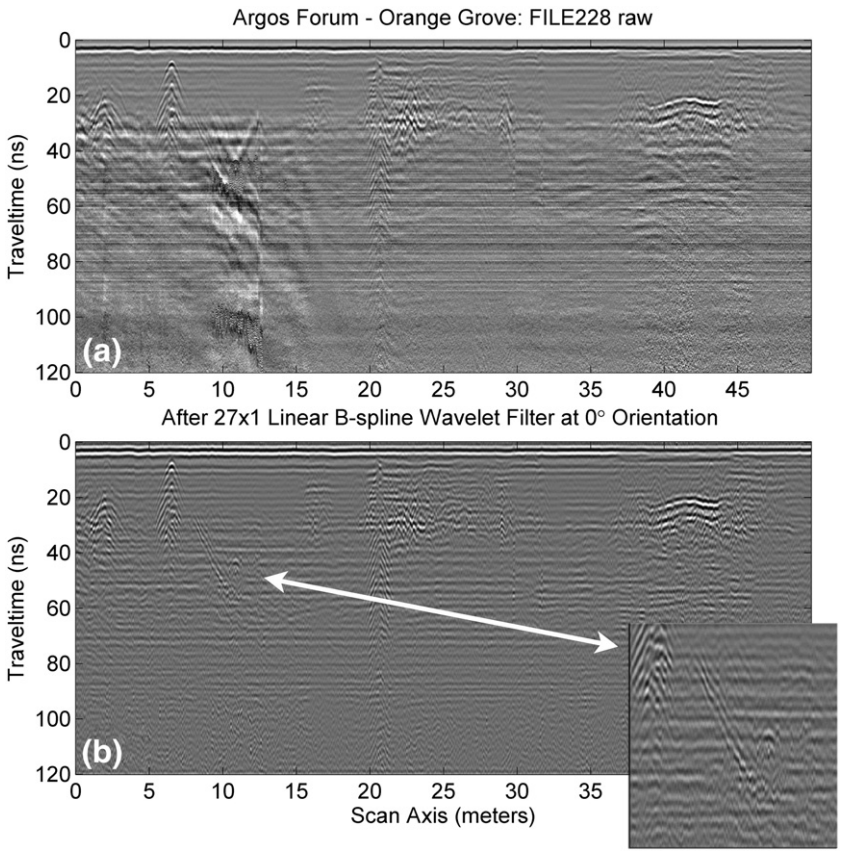

Fig. 4. (**a**) The raw radargram whence the trace of Fig. 3 was extracted; the trace is located at 9.62 m from the beginning of the section. (**b**) The same radargram after application of a 27-point linear B-spline wavelet tuned at 400 MHz. The inset figure shows (presumably) man-made structures previously obscured by the noise.

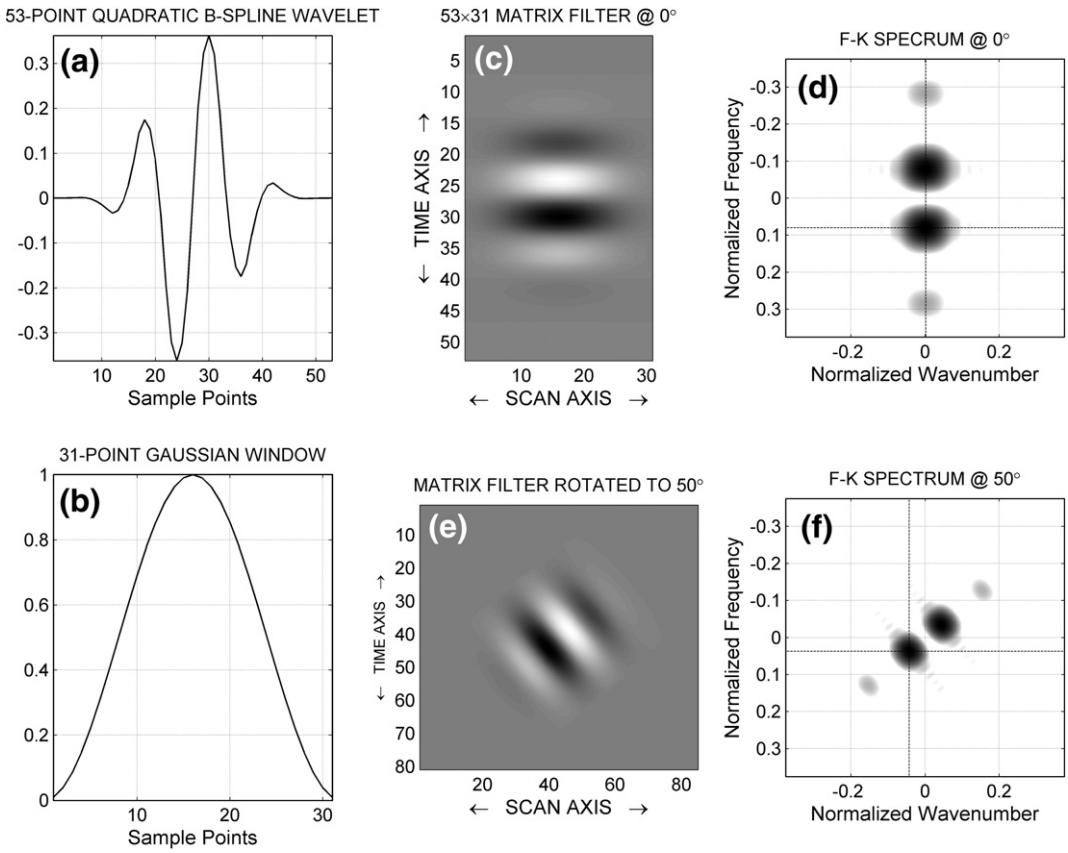

Fig. 5. Construction and spectral properties of a two-dimensional B-spline wavelet filter (see text for details).

span of the filter — equivalently the *aspect ratio* $\gamma = L/s$ — and the type of the smoothing window. The span determines the spatial extend over which to smooth: increasing (decreasing) the span contracts (expands) the lobes in the azimuthal direction and therefore influences spatio-temporal localization, but does not change the location of the peak, hence the resolvable data scale. The shape of the smoothing window influences the slope (roll-off rate) of the spectral lobes in the azimuthal direction and thus has a small effect on the temporal and spatial localization characteristics of the filter.

It is also easy to see that for $\theta \neq \varphi$, $\mathbf{b}(t^{\theta},x^{\theta}) \neq \mathbf{b}(t^{\varphi},x^{\varphi})$, therefore, $\mathbf{B}(f^{\theta},k^{\theta}) \neq \mathbf{B}(f^{\varphi},k^{\varphi})$ and $f^{\theta} \neq f^{\varphi}$, $k^{\theta} \neq k^{\varphi}$. Assuming that the data is collected at $\theta = 0°$, let the *reference peak frequency* for a filter of any given length be $f^{0}_{\max}$. As a result of the rotation, the peak moves away from its reference location and desired scale. In the example of Fig. 5, if the sampling rate is 1 s, then for $\theta = 0°$ the peak of the positive frequency lobe is located at $f^{0}_{\max} = 0.08$ Hz (Fig. 5d), while for $\theta = 50°$ it is located at $f^{50}_{\max} = 0.0371$ Hz (Fig. 5f). It follows that upon rotation by θ, in order for the peak to remain focused (tuned) on a given reference scale $f^{0}_{\max}$, one must adjust the length of the wavelet so that $f^{\theta}_{\max} \rightarrow f^{0}_{\max}$.

Fig. 6 shows examples of tuning the BSW Filter at a given temporal scale (reference frequency). Let us assume that the size of the radargram to be treated is 512×512 samples and that it has been obtained with a 400 MHz antenna, a sampling rate of 0.1957 ns and a trace spacing of 0.025 m. Also let the mother filter at $\theta = 0°$ be based on a Quadratic B-Spline wavelet and have a span of 21 points. Finally, let the target (reference) frequency $f^{0}_{\max}$ be equal to 400 MHz. For the mother filter ($\theta = 0°$) this will be achieved when $L = 54$ sample points along the time axis, thus resulting in a 54×21 matrix filter (Fig. 6a—top). At $\theta = 30°$, a Quadratic B-Spline/21-point Hanning Window filter will have $f^{30}_{\max} \approx 400$ MHz if the length of the mother filter (L) is reduced to 33 points (Fig. 6a—middle) and at $\theta = 60°$, it will have $f^{60}_{\max} \approx 400$ MHz if $L = 19$ points (Fig. 6a—bottom).

If the span remains constant, the aspect ratio changes and so does the shape of the spectral lobes. For the particular filter design of Fig. 6a, the spectral lobes change from oblate with respect to the radial direction at $\theta = 0°$ (Fig. 6a—top) to oblong at $\theta = 60°$ (Fig. 6a—bottom); this means that at low rotation angles the filter would tend to admit proportionally more arrivals from sub-horizontal interfaces, while at high rotation angles more arrivals from sub-vertical interfaces. In

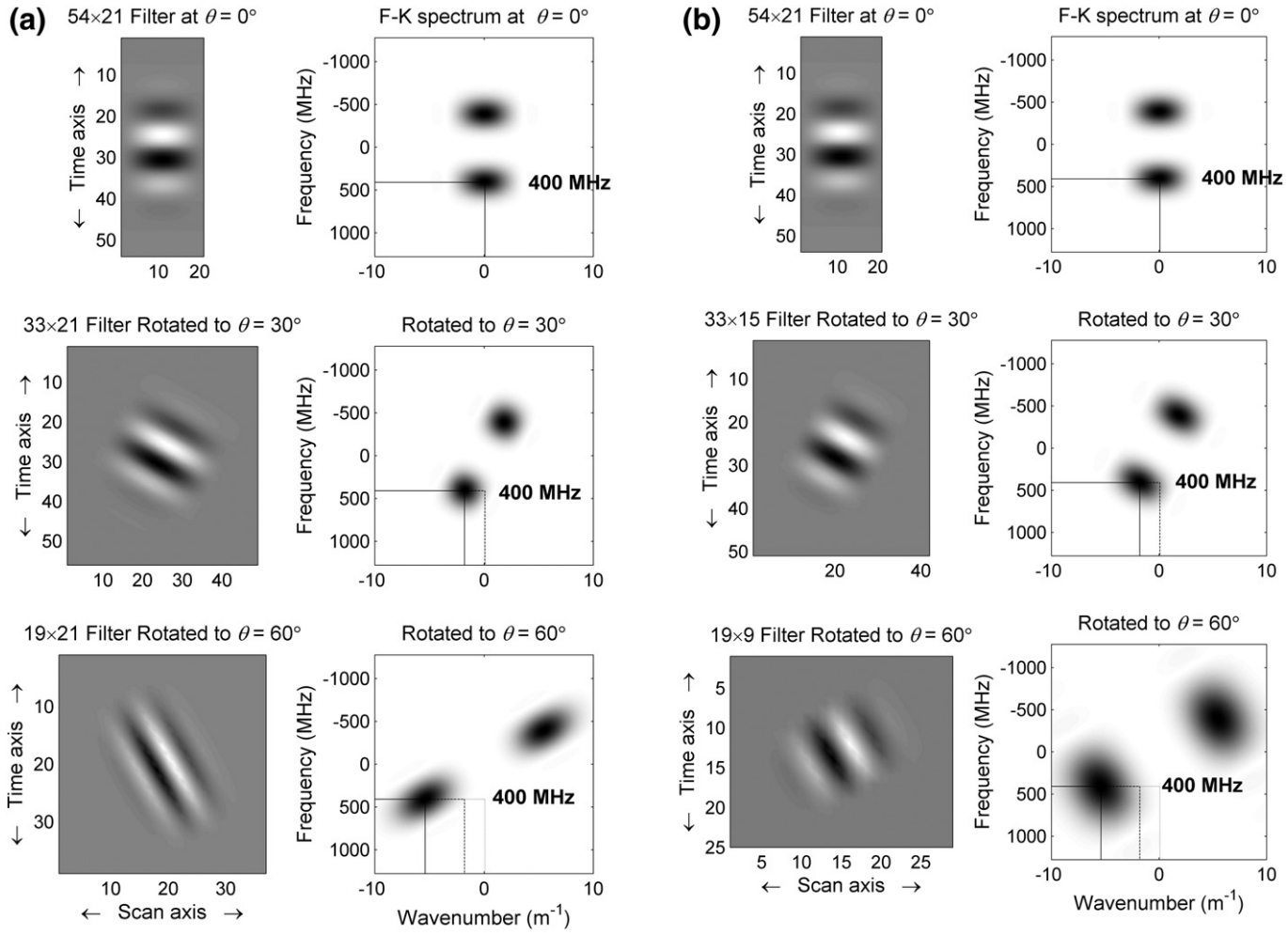

Fig. 6. a. Tuning a BSW filter at a given temporal scale (reference frequency) for different rotation angles. The basic design (*mother filter*) is a Quadratic B-spline/21-point Hanning Window matrix. If the tuning frequency is set to 400 MHz, then, for a rotation angle of $\theta = 0°$ the mother filter must be a 54 (length)×21 (span) matrix, for a rotation angle of $\theta = 30°$ a 33×21 matrix and for a rotation angle of $\theta = 60°$ a 19×21 matrix. **b.** Tuning a BSW filter at a given temporal scale (reference frequency) for different rotation angles while preserving the aspect ratio. The basic design (*mother filter*) is a Quadratic B-spline/21-point Hanning Window matrix. If the tuning frequency is set to 400 MHz, then, for a rotation angle of $\theta = 0°$ the mother filter must be a 54 (length)×21 (span) matrix with an aspect ratio of 2.57. For a rotation angle of $\theta = 30°$, the aspect ratio will be preserved if the mother filter is a 33×15 matrix; for a rotation angle of $\theta = 60°$ the aspect ratio will be preserved if the mother filter is a 19×9 matrix. **c.** Tuning a BSW filter at a given spatial scale (reference wavenumber) for different rotation angles. The basic design (*mother filter*) is a Linear B-spline/21-point Hanning Window matrix. If the tuning wavenumber is set to 2 m^{-1}, then for a rotation angle of $\theta = 90°$ the mother filter must be a 21 (span)×50 (length) matrix, for a rotation angle of $\theta = 60°$ a 21×33 matrix and for a rotation angle of $\theta = 30°$ a 21×18 matrix.

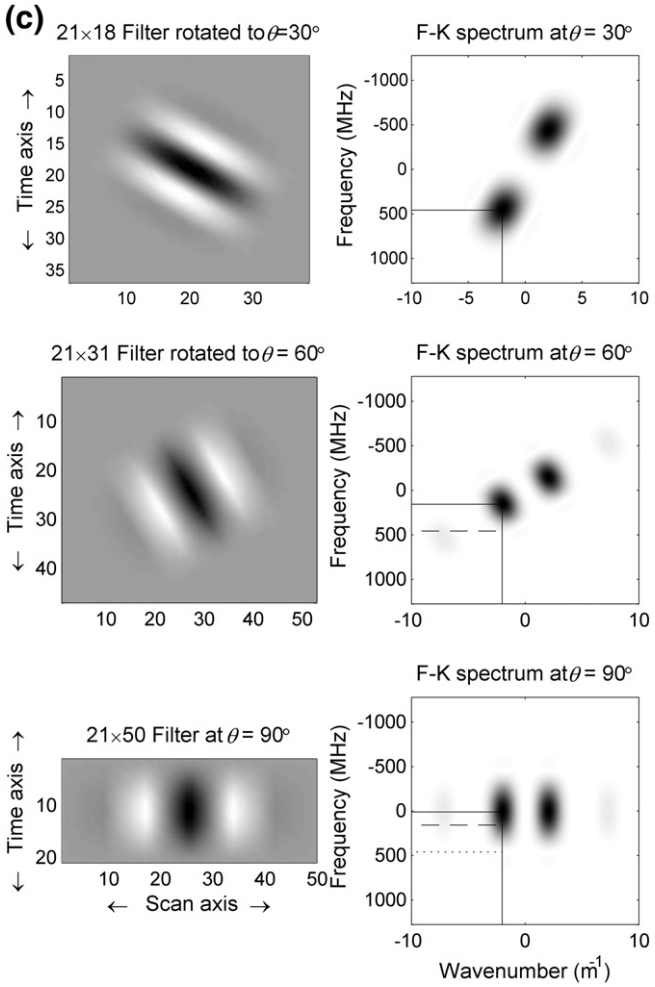

Fig. 6 (*continued*).

general, this would not be a problem, unless there is powerful interference from sources positioned sub-horizontally or sub-vertically with respect to the receiver, the latter being the more probable due to the nature of the GPR data. In such cases, the shape of the spectral lobes can be preserved by adjusting the span, so as to preserve the aspect ratio of the mother filter. In the example of Fig. 6b the aspect ratio of the 54×21 mother filter (Fig. 6b—top) is preserved, along with the shape of the spectral lobes, if at $\theta=30^\circ$ the span is reduced to 15 points (Fig. 6b—middle) and at $\theta=60^\circ$ to 9 points (Fig. 6b—bottom). The downside of this process is that the half-response bandwidth expands at high rotation angles (the spectral lobes broaden), due to the overall contraction of the BSW Filter. Experience with using the filter, however, shows that this is of little practical consequence for its performance.

It is important to note that this type of tuning breaks down as the rotation angle approaches $\pm 90^\circ$ because the filter becomes prohibitively short. The breakdown occurs abruptly at an angle dependent on the sampling interval. A remedy would be to resample the data at higher rates, or to use higher order wavelets (albeit at the expense of higher localization). Nevertheless, there is still a limit beyond which the tuning procedure is impractical: this is at rotation angles of approx. $\pm 90^\circ \pm 5^\circ$. As, however, will be argued in Section 7 (Epilogue), this does not pose practical limitations to the resolving power of the method.

The same procedure can be applied for tuning the BSW Filter at a given *reference wavenumber*. The difference here is that the mother filter must be defined at the angle $\theta=90^\circ$, so that the span will align with the time axis. Let the reference wavenumber be $k^{90}_{\max}=2\ \mathrm{m}^{-1}$. Fig. 6c—bottom shows the mother filter which is based on a Linear B-Spline wavelet and has a span of 21 points. At $\theta=90^\circ$ this filter will tune at the reference wavenumber for $L=50$. At $\theta=60^\circ$ the filter will remain tuned at the reference wavenumber if L is reduced to 31 points (21×31 mother filter, Fig. 6c—middle) and at $\theta=30^\circ$ if $L=18$ points (21×18 mother filter, Fig. 6c—top). As per Fig. 6a, if the span remains constant, the aspect ratio changes and the shape of the spectral lobes changes accordingly. Again as per Fig. 6b, the shape of the spectral lobes can be preserved by changing the span. Details will not be shown for the sake of brevity.

It is also important to note that wavenumber tuning breaks down as the rotation angle approaches 0° and 180° because the filter again becomes prohibitively short. The breakdown occurs abruptly at an angle dependent on trace spacing. An analogous remedy would be to resample the data at shorter spacing, or to use higher order wavelets but this would still leave a range of approx. $0^\circ \pm 5^\circ$ and $180^\circ \pm 5^\circ$ where the tuning procedure would be impractical. Again, as will be argued in Section 7, this does not pose practical limitations to the resolving power of the method.

It is straightforward to automate the determination of the optimal wavelet length L. Let

$$\chi_\odot = \begin{cases} f^0_{\max} > 0 \\ k^{90}_{\max} > 0 \end{cases}$$

be the target (reference) frequency or wavenumber. Also let

$$\chi^\theta_\odot = \begin{cases} \left|\hat{f}^\theta_{\max}(L)\right| \\ \left|\hat{k}^\theta_{\max}(L)\right| \end{cases}$$

be the abscissa or ordinate of the peak of the spectral lobe that lies in the positive frequency or wavenumber half-plane, for a rotation angle θ and length L. If one would like to preserve the aspect ratio this definition would have to be modified thus:

$$\chi^\theta_\odot = \begin{cases} \left|\hat{f}^\theta_{\max}(L, s(L))\right| \\ \left|\hat{k}^\theta_{\max}(L, s(L))\right| \end{cases}.$$

Then, the optimal L can be obtained by minimizing a simple loss function of the form

$$\rho(L) = \left|\chi_\odot - \chi^\theta_\odot\right|.$$

3.1. Example

The data of Fig. 7a was collected as part of the Argos archaeometric survey (see above), with a GSSI SIR-2000 system and an antenna with a nominal central frequency of 400 MHz. The raw radargram is shown as measured: it is quite noisy and comprises a 512 sample×1024 traces section with a sampling rate of 0.1957 ns (total time window = 100 ns) and trace spacing 0.01075 m (section length = 11 m). One apparent and significant feature in this section is an up-dipping reflector which is clearly seen between the coordinates (60 ns, 6 m) and (49 ns, 7.8 m), while there is quite clear indication that it may extend bilaterally to later times/shorter distances (approx. 66 ns/5 m) and earlier times/longer distances (approx. 37 ns/10 m).

The design of a BSW Filter to extract the reflector can be based on a few simple considerations: The main pulse of this reflection shows a positive–negative–positive polarity sequence and its duration can be measured at a few locations: the time between the positive peaks averages at 1.76 ns. This is clearly an event rich in high frequencies — if it was a sinusoid, it would have a frequency of approx. 570 MHz. Conversely, the width of the pulse parallel to the scan line can be considered, although in this case it is rather difficult to measure due to the intense interference parallel to the scan line. At any rate, it can be estimated in the range 0.19 m to 0.32 m with an average at

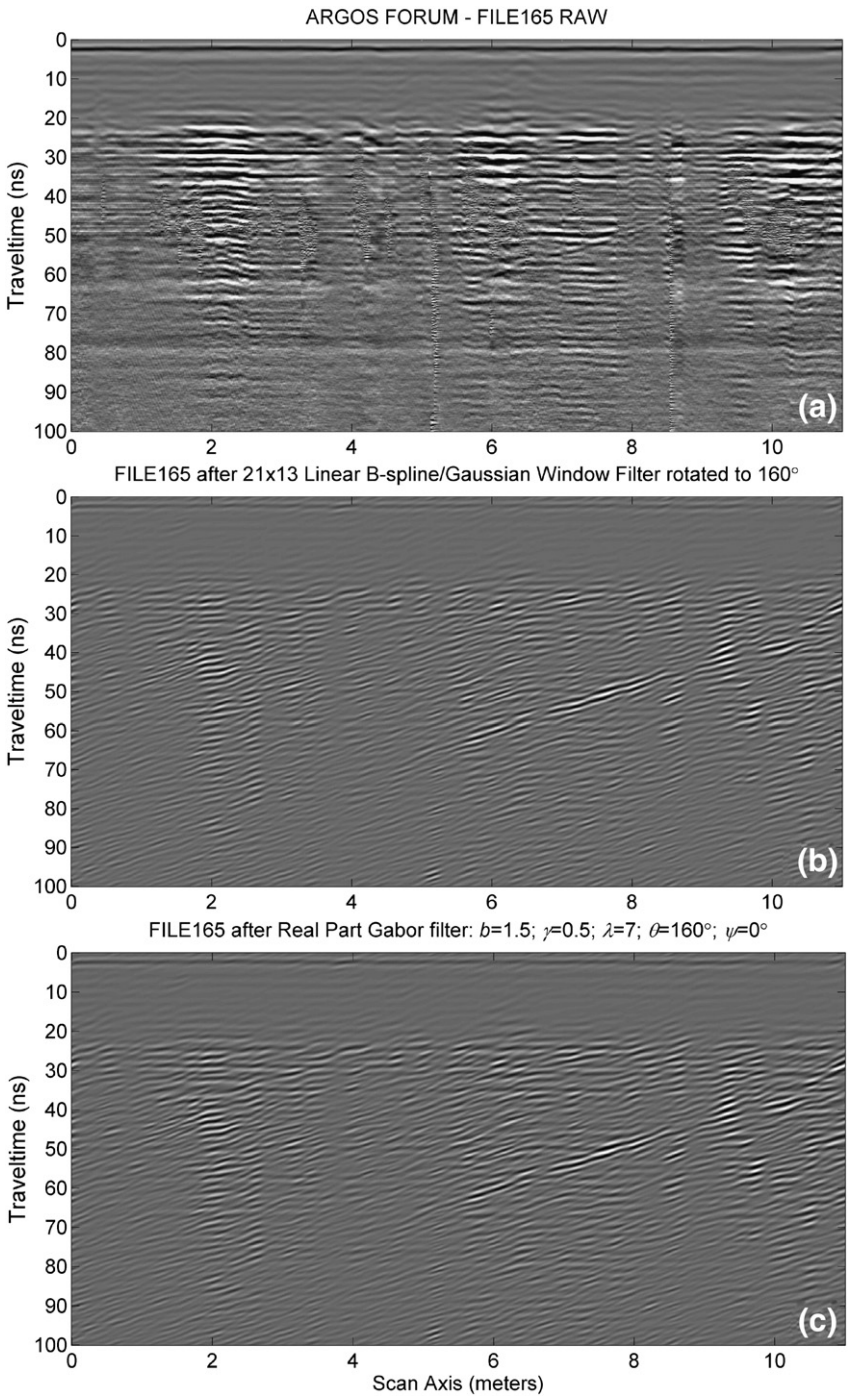

Fig. 7. (a) B-scan radargram featuring a linear up-dipping reflector between the ordinates 49–60 ns and abscissae 6–7.8 m buried in noise. There is compelling indication that the reflector may extend bilaterally to later times/shorter distances and earlier times/longer distances. **(b)** The same radargram after application of a 21×13 Linear B-spline/Gaussian window mother filter rotated to $\theta=160°$, so that the wavenumber would be tuned at $k=4.16$ m^{-1}. **(c)** The same radargram after application of a Gabor filter with design parameters $b=1.5$, $\gamma=0.5$, $\lambda=7$ and $\theta=160°$; the wavenumber is tuned at the reference scale of $k=4.15$ m^{-1}.

0.24 m. This implies spatial wavenumbers in the range 5.3 m^{-1} to 3 m^{-1} with an expectation value of 4.2 m^{-1}. Notably, tuning of the filter at both the expectation frequency and wavenumber is possible only in a narrow range of rotation angles around 20° and 160°. Given this information, one may design the filter in three ways:

i. Estimate the dip angle, rotate the filter to an angle perpendicular to the dip and vary the length until it is tuned at the expectation frequency.
ii. Estimate the dip angle, rotate the filter to an angle perpendicular to the dip and vary the length until it is tuned at the expectation wavenumber.
iii. Vary the length and rotation angle until the filter is tuned at both the expectation frequency and wavenumber; the final rotation angle should be approximately perpendicular to the dip.

After the filter is tuned to the expectation values, one may experiment by adjusting the length, span and rotation angle, until an “optimal” result

is obtained. This is because the span of the filter inversely affects its spatial localization properties. In the inevitable absence of an objective measure, (for instance in the form of a simple metric), the optimality of the output is a matter of expert judgment in relation to the objective of the application.

One such optimal result is shown in Fig. 7b, after treating the radargram with a 13×21 Linear B-Spline/Gaussian window filter rotated to $\theta = 160°$, so that the frequency is tuned at 628 MHz ($f_{\max}^{160} = 628$ MHz) and the wavenumber at 4.16 m^{-1} ($k_{\max}^{160} = 4.16\ m^{-1}$). The dipping reflector stands out clearly and its lateral extent beyond the initially observable range is confirmed.

In addition to the "apparent" reflection discussed above, the filter detects a "hidden" reflector with similar geometrical characteristics between (40 ns, 1.3 m) and (23 ns, 4.2 m). This feature deserves some scrutiny because in the raw data it is heavily obscured by other powerful reflection events and noise, so that it can be observed only after careful inspection. Consider that the BSW Filter is highly selective; if parts of the data contain geometrical components associated with a specific orientation, the filter will pick them out and obliterate any irrelevant information. However, if these components do not belong to an extended dipping reflector, they will either be unorganized and scattered (noise), or they will be arranged vertically as a consequence of them having been produced by sharp lateral changes in buried structures (e.g. walls) or noise (e.g. ringing). In Fig. 7b one may observe several "small" dipping reflections that exhibit such traits. In the case of the "hidden reflector" however, they are arranged along a single dipping line for an extended part of the section. This is hardly a coincidence; rather, it is the signature of a dipping interface with apparently weak reflectivity, obscured by interference of higher intensity. In a final comment, note that the "hidden reflector" is for real — it can be observed with the same characteristics in neighbouring parallel sections and over the same span as the deeper, apparent reflector. In this particular section it happened to be heavily obscured, which is why it was selected for demonstration.

4. Two-dimensional Gabor Wavelet Filters

A 2-D Gabor Filter is a Gaussian kernel function modulated by a sinusoidal plane wave. Its impulse response is defined by a harmonic function multiplied by a Gaussian function (Gabor function). The filter has a real and an imaginary component representing orthogonal directions. The two components may be formed into a complex quantity or be used individually. Details can be found in the abundant pertinent literature, as for instance are the monographs edited by Feichtinger and Strohmer (1998, 2003) and the numerous contributions therein. The parameterization adopted herein follows the formulation proposed by Daugman (1985) and further developed by Kruizinga and Petkov (1999), Grigorescu et al. (2002), Grigorescu et al. (2003) and others, at the Institute of Mathematics and Computing Science, University of Groningen (Netherlands):

$$\mathbf{g}(x,t;\lambda,\theta,\psi,\sigma,\gamma) = \exp\left(-\frac{\left(x^{\theta}\right)^2+\gamma^2\left(t^{\theta}\right)^2}{2\sigma^2}\right)\exp\left(j\left(2\pi\frac{x^{\theta}}{\lambda}+\psi\right)\right) \tag{4a}$$

where

$$\begin{aligned} x^{\theta} &= x\cos\theta + t\sin\theta \\ t^{\theta} &= -x\sin\theta + t\cos\theta. \end{aligned} \tag{4b}$$

The parameter λ represents the wavelength of the sinusoidal factor, θ represents the orientation of the normal to the parallel stripes of a Gabor function (e.g. Feichtinger and Strohmer, 1998, 2003), ψ is the phase offset, σ is the standard deviation of the Gaussian factor and γ is the spatial aspect ratio which specifies the ellipticity of the support of the Gabor function. For $\gamma = 1$ the support is circular. For $\gamma < 1$ the support is oblong in the orientation of the parallel stripes of the Gabor function (i.e. in the azimuthal direction). For $\gamma > 1$ the support is oblong perpendicularly to the orientation of the parallel stripes of the Gabor function (i.e. in the radial direction). The half-response spatial frequency bandwidth b of a Gabor Filter (in octaves) is related to the ratio σ/λ as follows:

$$b = \log_2\left(\frac{\frac{\sigma}{\lambda}\pi+\sqrt{\frac{\ln 2}{2}}}{\frac{\sigma}{\lambda}\pi-\sqrt{\frac{\ln 2}{2}}}\right), \quad \frac{\sigma}{\lambda} = \frac{1}{\pi}\sqrt{\frac{\ln 2}{2}}\cdot\frac{2^b+1}{2^b-1}$$

Thus, the value of σ may not be specified directly and may be set through the more intuitive parameter b. The smaller the bandwidth, the larger is σ, the support of the Gabor function and the number of visible parallel excitatory and inhibitory stripe zones.

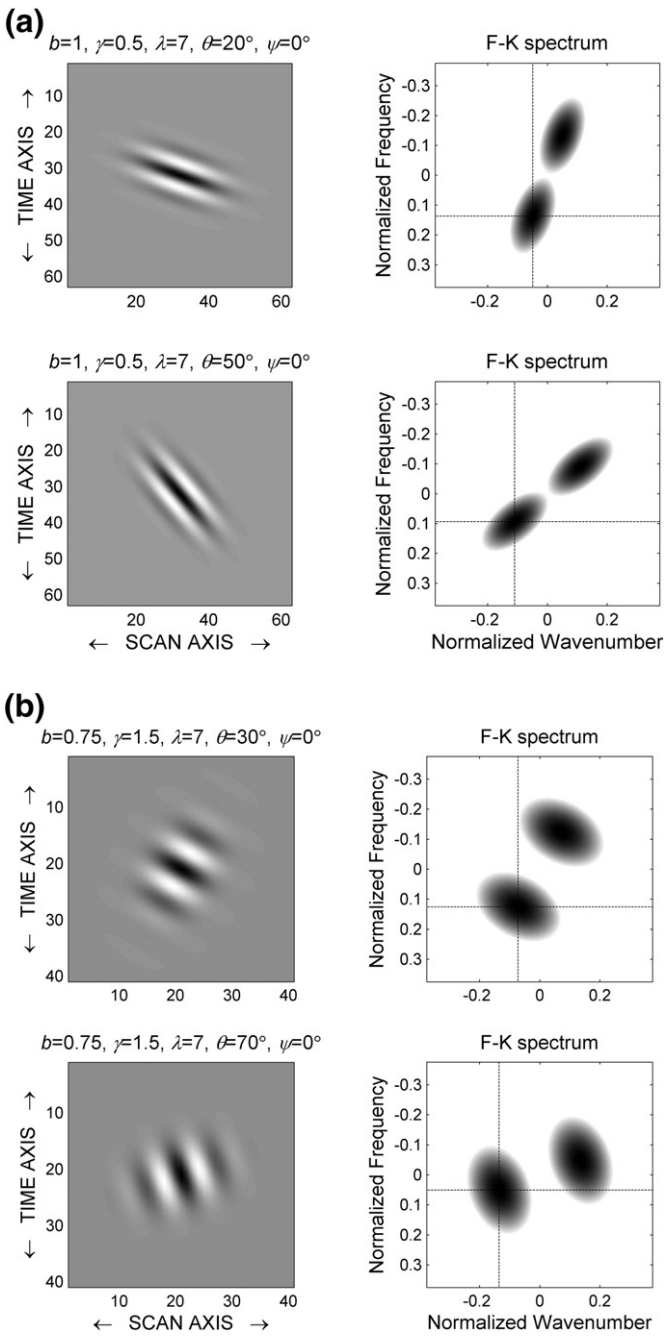

Fig. 8. a. A Gabor filter with aspect ratio $\gamma < 1$ at different rotation angles. **b.** A Gabor filter with aspect ratio $\gamma > 1$ at different rotation angles.

Because of the convolution theorem, the Fourier transform of the impulse response is the convolution of the Fourier transform of the Gaussian kernel and the Fourier transform of the sinusoidal term. Both transforms can be computed analytically (in the rotated co-ordinate system). The Gaussian kernel gives:

$$\mathbf{G}_g\left(f^\theta,k^\theta\right)=\frac{2\pi\sigma^2}{\gamma}\exp\left(-2\pi^2\sigma^2\left[\left(k^\theta\right)^2+\frac{\left(f^\theta\right)^2}{\gamma^2}\right]\right).$$

The f–k transform of the modulation term can also be computed analytically:

$$\mathbf{G}_S\left(f^\theta,k^\theta\right)=2\pi\cdot\exp(i\psi)\cdot\delta\left(2\pi k^\theta+\frac{2\pi}{\lambda}\right),$$

where δ is a Dirac delta sequence function. The convolution of these two expressions gives the analytic form of the Gabor f–k spectrum

$$\mathbf{G}\left(f^\theta,k^\theta\right)=\frac{4\pi^2\sigma^2}{\gamma}\exp\left(-2\pi^2\sigma^2\left[\left(k^\theta\right)^2+\frac{\left(f^\theta\right)^2}{\gamma^2}\right]\right)\cdot\exp(i\psi)$$

It is easy to see that this function consists of two lobes symmetric with respect to the origin and that the f–k and t–x representations of the Gabor Filter have identical orientations. For $\gamma=1$ the lobes are circular. For $\gamma<1$ the lobes are oblong in the radial direction (Fig. 8a). For $\gamma>1$ the lobes are oblate in the radial direction (Fig. 8b). It is also straightforward to verify that owing to the scaling properties of the Gabor wavelet, the coordinates of the peaks of the spectral lobes are determined exclusively by the wavelength λ, which thus defines the temporal or spatial scale to be isolated. The width of the pass-band and the sharpness (roll-off rate) of the spectral lobes are determined by the bandwidth b, while the span of the filter (size of the smoothing window) is determined by the aspect ratio γ. In consequence, the combination bandwidth/aspect ratio controls the dilation or contraction of the filter, hence the amount of information allowed through the filter at the given scale. With respect to the BSW Filters discussed above, the length of the B-Spline wavelet corresponds to the wavelength of the Gabor Filter and the combination span/smoothing window to the combination bandwidth/aspect ratio.

Also as above, for $\theta\neq\varphi$, $\mathbf{g}(x^\theta,t^\theta)\neq\mathbf{g}(x^\varphi,t^\varphi)$, therefore, $\mathbf{G}(f^\theta,k^\theta)\neq\mathbf{G}(f^\varphi,k^\varphi)$ and $f^\theta\neq f^\varphi$, $k^\theta\neq k^\varphi$. Again assuming that the data is collected at $\theta=0°$, the *reference scale* (peak frequency/wavenumber) for a given wavelength λ are $f^0_{\max}$ or $k^{90}_{\max}$ respectively. At any $\theta\neq0$, the peak moves away from its reference location, thus changing the selectable scale. It follows that in order for the peak to remain focused on a given reference scale, one must adjust λ so that $f^\theta_{\max}\to f^0_{\max}$ or $k^\theta_{\max}\to k^{90}_{\max}$.

Gabor Filters are directly related to Gabor wavelets, since they can be designed for different dilations and rotations. The most usual application is to create a filter bank with various scales and rotations, which are convolved with the signal, resulting in a so-called Gabor space. Last, but not least, the Gabor Filters and B-Spline wavelets are closely related. In fact, Unser (1992) has shown that B-Spline wavelets converge to Gabor functions (modulated Gaussian) pointwise and in all L^n-norms with $1\leq n<+\infty$ as the order of the spline tends to infinity; the approximation error for the cubic B-Spline wavelet is already less than 3%. The exact relationship between the BSW Filter and the Gabor Filter will not be investigated in the context of this presentation.

Fig. 7c illustrates the output of a 2-D (real part) Gabor Filter operating on the data of Fig. 7a. The design parameters were $b=1.5$, $\gamma=0.5$, $\lambda=7$ and $\theta=160°$, so that the filter is exactly parallel to the hidden reflection and the wavenumber tuned at the reference scale of $k^{90}=4.15\ \mathrm{m}^{-1}$. The result is absolutely comparable to that of Fig. 7b: the primary dipping reflector stands out clearly and its lateral extent beyond the originally observable range is also confirmed. The second reflector between coordinates (40 ns, 1.3 m) and (23 ns, 4.2 m) is also efficiently detected.

5. Scale and geometrical feature extraction — de-noising

In the general case a radargram may contain reflections from variable-dip reflectors, multiple reflectors with different dips, etc. A single-dip BSW or Gabor Filter will extract only part of the available dip-dependent information because it is highly selective. Although the high selectivity is desirable if one wishes to isolate scale-and-dip dependent information, it is very restrictive when one wishes to extract scale-dependent information only, over a broad or narrow range of dips (multiple- or variable-dip geometric features). In such cases, a more sophisticated approach is required. The application of directional filters to image processing (e.g. edge and contour detection) often involves the combination of partial images obtained by application of the same filter rotated to different directions (e.g. see Freeman and Adelson, 1991, for Steerable Wavelets, or Grigorescu et al., 2003, for Gabor Filters). This procedure is fine for common images, where both dimensions are of the same nature (spatial) and the location of the peak remains locked at a constant radius during rotation. However, it may not be always suitable for GPR data, where the dimensions are of different nature (one temporal and one spatial).

The solution proposed herein borrows insight from the techniques used in edge detection, but with adaptations that render them suitable for GPR data. Letting $\mathbf{D}$ be the f–k transform of the data and $\mathbf{F}$ the normalized f–k transform of the filter at angle θ and length L, so that $\mathbf{F}(\theta,L)=\mathbf{B}(\theta,L)\cdot\|\mathbf{B}(\theta,L)\|_\infty^{-1}$ or, $\mathbf{F}(\theta,L)=\mathbf{G}(\theta,L)\cdot\|\mathbf{G}(\theta,L)\|_\infty^{-1}$, the proposed procedure entails:

i) Application of the BSW or Gabor Filter rotated to different angles under adaptive control so that it will remain tuned at a given frequency or wavenumber. This will yield a series $j=1,\ \ldots\ N$ of orientation-dependent outputs:

$$\hat{\mathbf{D}}_j\left(\theta_j,\chi_\odot\right)=\mathbf{D}\cdot\mathbf{F}\left\{\theta_j,L_j:\left|\chi_\odot-\chi^\theta_\odot\right|\to0\right\}$$

ii) Stacking of the orientation-dependent outputs in the weighted least-squares sense

$$\bar{\mathbf{D}}(\theta_1:\theta_N,\chi_\odot)=\left[\sum_{j=1}^{N}\hat{\mathbf{D}}_j\left(\theta_j,\chi_\odot\right)\cdot w\left(\theta_j,\chi_\odot\right)\right]\cdot\left[\sum_{j=1}^{N}w\left(\theta_j,\chi_\odot\right)\right]^{-1}.$$

The stacking weight can have several forms — the weights implemented herein are generally functions of a measure of the energy contained in the output data normalized by the same measure of the energy contained in the input data in the sense:

$$w\left(\theta_j,\chi_\odot\right)=\|\hat{\mathbf{D}}\left(\theta_j,\chi_\odot\right)\|_n\cdot\|\mathbf{D}\|_n^{-1},$$

where n can be 1 (Manhattan norm), 2 (Euclidean norm), or ∞ (infinity norm). It is also possible to set $w(\theta_j,\chi_\odot)=1$, (i.e. obtain a straight arithmetic average of the outputs at different rotation angles). This weighting scheme guarantees that the final output will not be disproportionally dominated by powerful spectral components and that it will be a faithful representation of the scale-dependent information originally contained in the input data. Moreover, the stacking will tend to smear dip-dependent noise features eluding the filter at a given temporal or spatial scale, further enhancing the S/N ratio.

The filtering scheme described above facilitates the combination of several "partial" (same-scale-and-dip-dependent) data subsets into an image that is scale-dependent but dip-independent over an arc $\widehat{\theta_1\theta_N}$. The output image will account for any variation in the angle of dip, including the case of (smoothly or sharply) curved

interfaces. In order to demonstrate how this process works, a number of characteristic examples will now be provided.

5.1. Examples

The first example may be familiar to several GPR practitioners: it is the radargram distributed with the GPR analysis package of Lucius and Powers (2002). The original section was measured in B-scan equal time spacing mode at the Norman (Oklahoma) Landfill with a GSSI SIR-2000 system and a 500 MHz low power antenna; it was subsequently pre-processed (transformed to equal trace spacing and resampled to 1024 samples × 1024 traces), so that it now has a sampling rate of 0.099 s (time window equals to 101.7 ns) and a trace spacing of 0.0194 m (section length is 19.8 m). The section is shown in Fig. 9 and can be seen to suffer from crossing clutter, characteristic of multiple small targets or rough reflective surfaces. The noise can be locally strong, but it does not completely overshadow the data which is still interpretable; this is one reason why this example was chosen: the performance of the adaptive filtering process can be precisely evaluated because the observer can see exactly what lies behind the noise.

The clutter waveforms have short spatial widths which can be roughly measured at several locations on the radargram (see also Section 3.1): they average to approx. 0.25 m, which would imply expected wavenumber(s) of the order of 4 m^{-1}. It is then possible to tune a BSW Filter at these wavenumber(s), so as to isolate the clutter. The optimal aspect ratio can be decided through experimentation. Fig. 10a illustrates a model of the clutter derived by an adaptive Quadratic B-Spline/5-point Hanning Window filter sweeping the arc [10°, 170°] in steps of 10° while tuned at $k=4$ m^{-1}. The span of the filter was kept short (5 points) in order to maintain high spatial resolution.

It is also possible to obtain noise-free data without significant loss of information. A simple inspection of the data will show that the main reflections from subsurface interfaces have spatial widths (scales) of metric order. Likewise, an inspection of individual trace spectra, as well as of the *f*–*k* spectrum will show that the data is disproportionally rich in low frequencies, with the peak located in the neighbourhood of 300 MHz (on average). Accordingly, the de-noising filters can be tuned at spatial scales of metric-order, or temporal scales significantly longer than those corresponding to the nominal central frequency of the antenna (300–400 MHz). To this effect, Fig. 10b illustrates a representation of the data after application of a Linear B-Spline/11-point Hanning Window filter tuned at $k=1$ m^{-1} over the arc [10°, 170°]. Fig. 10c is the same for a Linear B-Spline/21-point Hanning Window filter tuned at 350 MHz over the arc [−80°, 80°]. It is noteworthy that the more significant volume of Earth-structural information is recovered at longer wavelengths and lower frequencies and this may be telltale of the ground conditions through which the signal propagates. This issue will be revisited in the next example, after additional observations have been presented.

The second example data set was collected with a Måla GPR system and 250 MHz antenna on a ridge (Mt Ktenias, altitude ~1600 m, NE Peloponnesus, Greece), where high-rising wind-powered electricity generators were to be erected, as part of a geotechnical survey to investigate the conditions and consistency of the foundation ground (e.g. to detect voids). This radargram has also been presented and treated by Tzanis (2010), as an illustratory example of the matGPR software. The geological setting is shown in Fig. 11. The ground comprises dipping, thin-plated limestone with intercalations of argillaceous material, intensely fragmented and karstified (as in Fig. 11b, c and d). The fragmentation of the limestone is due to faulting and (apparently) multi-phase jointing. Karstification has subsequently nucleated at the loci of faults and major joints. As evident in the photographs, many cracks and voids are filled with lateritic material with a considerable argillaceous component. Fig. 12a shows the example section after time-zero adjustment, global background removal, AGC with a 20 ns Gaussian-tapered window and elimination of antenna self-clutter (see Tzanis, 2010). The later parts of the data traces, (after approx. 80 ns), are infested with apparently random noise which is amplified by the AGC and may mask other useful reflections. Fig. 12b is the same data after *F*–*K* time migration — this is the actual data set used in the ensuing analysis.

The existence of numerous linear or quasi-linear reflection events with variable length and dip can be easily recognized at several locations in Fig. 12. These may be due to small aperture fractures and joints as well as due to the bedding (as per Fig. 11a and c). Since the detection of fractures has always been a major application of GPR, this data is suitable for demonstrating the applicability of the adaptive filtering procedure to such problems. Careful inspection of the data shows that there are two kinds of linear reflections with different and measurable spatial widths that cluster around approx. 0.27 m and 0.5 m. This would imply the existence of two kinds of fractures with different aperture, respectively associated with expected wavenumbers of the order 4 m^{-1} and 2 m^{-1}. This possibility can be investigated with rotating BSW Filters tuned at the different wavenumbers.

Fig. 13a illustrates the information extracted from the data of Fig. 12b by a Quadratic B-Spline/11-point Hanning Window filter sweeping the arc [20°, 160°] in steps of 10° and tuned at $k\approx4$ m^{-1}. Likewise, Fig. 13b illustrates the information extracted by a Quadratic B-Spline/11-point Hanning Window filter sweeping the arc [10°, 170°] in steps of 10° and tuned at $k\approx2$ m^{-1}. In both cases, the quadratic B-Spline and the

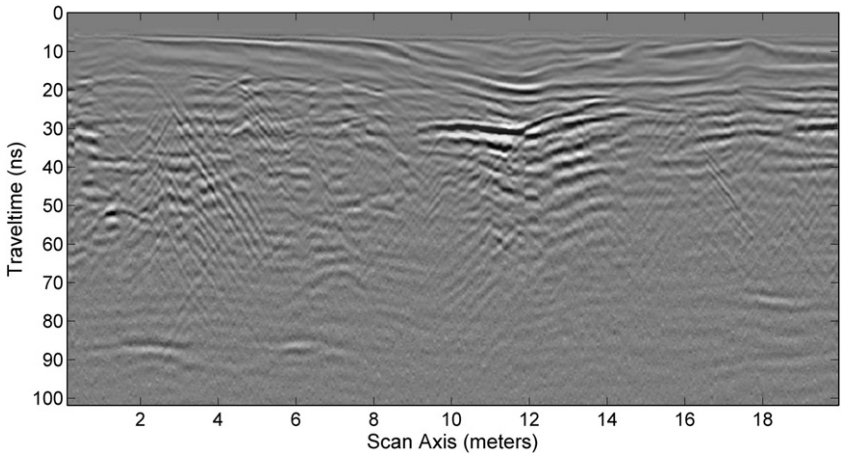

Fig. 9. The B-scan radargram distributed with the GPR analysis package of Lucius and Powers (2002), transformed to equal trace spacing and resampled to a 1024 × 1024 matrix. The data suffer from crossing clutter, characteristic of multiple small targets or rough reflective surfaces.

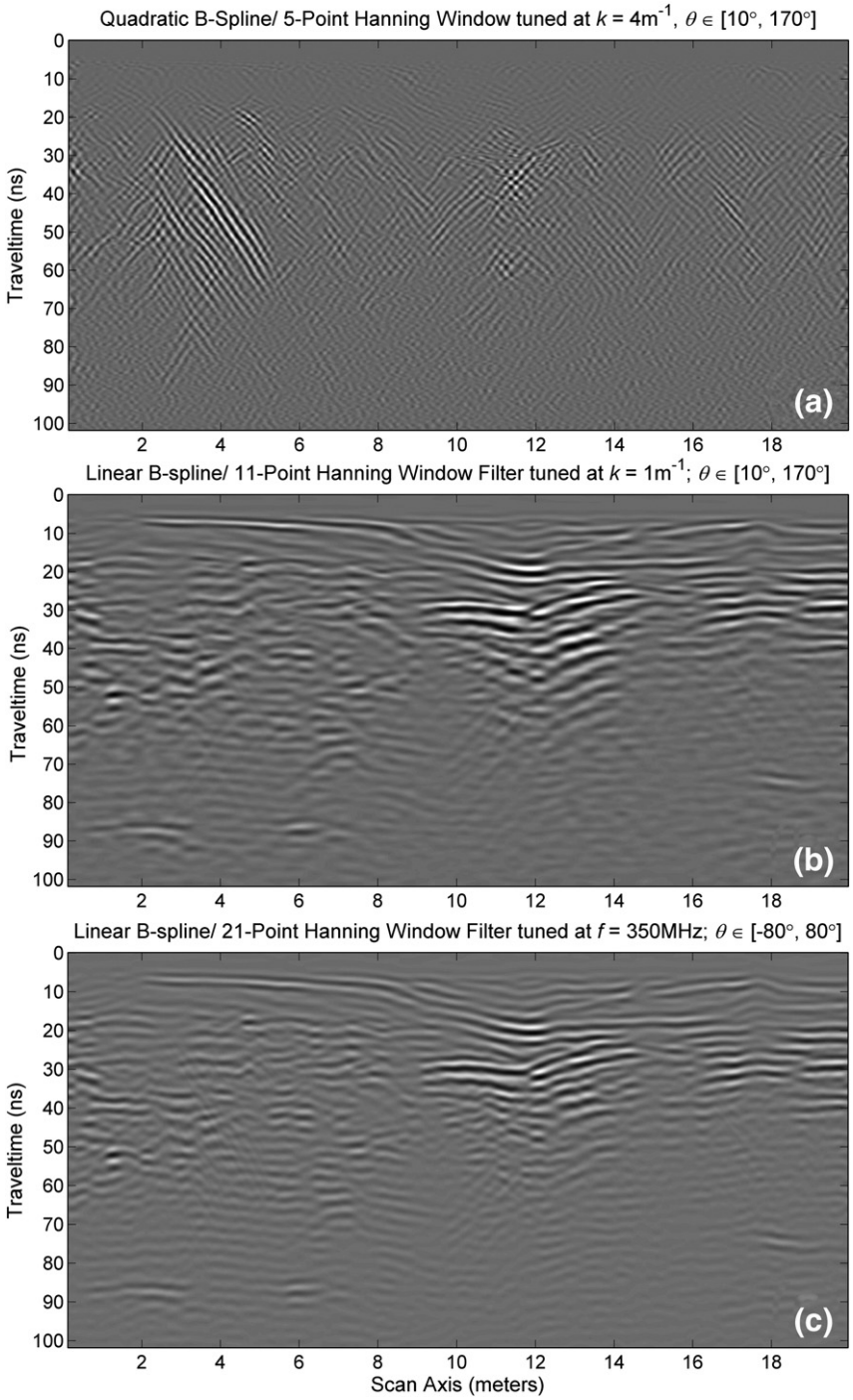

Fig. 10. (**a**) The data of Fig. 9 after application of a Quadratic B-spline/5-point Hanning Window filter sweeping the arc [10°, 170°] in steps of 10° while tuned at $k=4\ m^{-1}$. This application effectively isolates the crossing noise process. (**b**) The same data after application of a Linear B-spline/11-point Hanning Window filter sweeping the arc [10°, 170°] while tuned at $k=1\ m^{-1}$. This application yields a representation of noise-free data. (**c**) The same data after application of a Linear B-spline/21-point Hanning Window filter sweeping the arc [−80°, 80°] while tuned at $f=350$ MHz. This application yields an alternative representation of noise-free data.

relatively short span were selected in order to maintain moderate — high spatial localization. It is apparent that the filter tuned at the longer wavenumber (Fig. 13a) detects mainly steep linear reflections; these are both down- and up-dipping and will henceforth be referred to as "Type A reflections". The filter tuned at the shorter wavenumber (Fig. 13b) picks out the shorter wavelength components of Type A reflections, but also detects out a second set of gently dipping linear reflections, henceforth to be called "Type B reflection." These are generally closely spaced, almost entirely down-dipping, and cannot be observed at times longer than 80 ns approx.

Type A reflections exhibit consistent angular relationship and dip at $\pm 50°$ to $\pm 60°$: they correspond to joints and to synthetic and antithetic fractures.[1] They cannot be classified as faults due to the apparent absence of displacement between the foot and hanging walls, as observed both in the field and the GPR section. The largest representative of this group is the steep up-dipping series of aligned

[1] These, and all subsequent angle measurements were conducted on a depth migrated section which is not shown for the sake of brevity and were verified by field observations (also see Fig. 11).

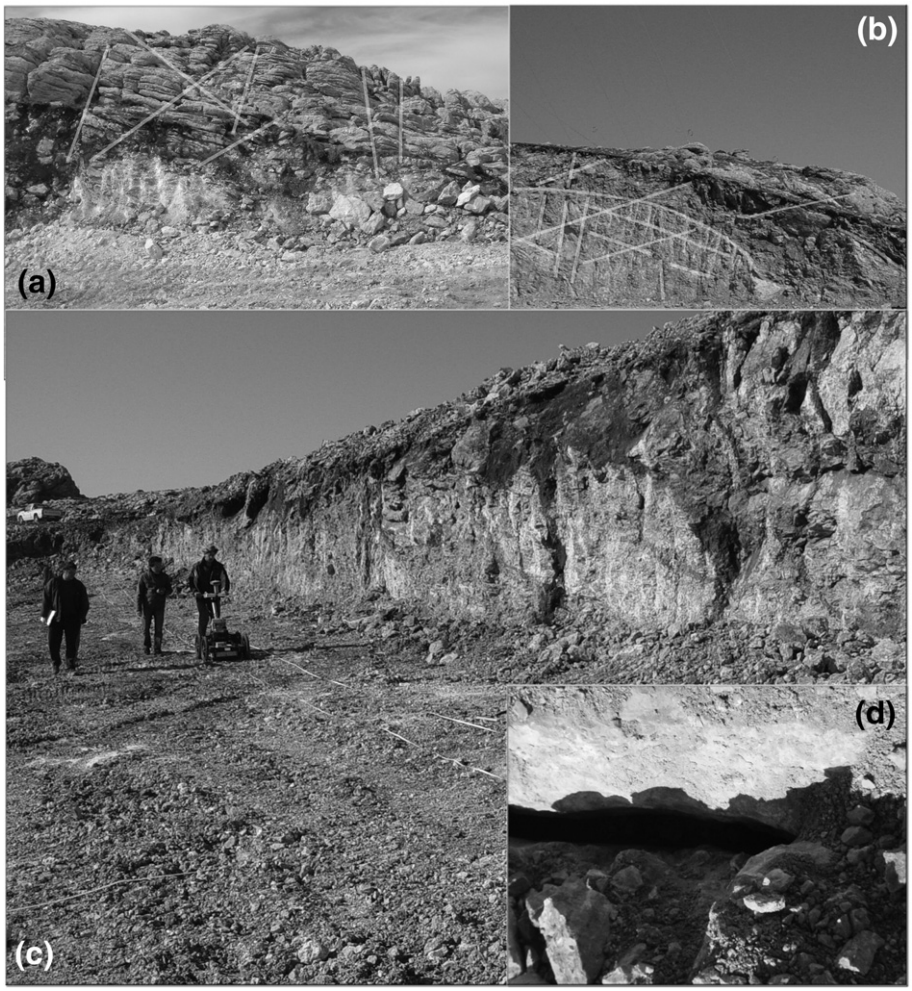

Fig. 11. The geological setting of the Ktenias ridge. **(a)** Damaged thin-plated limestone with fractures and joints. **(b)** Heavily fragmented and damaged limestone block overlying healthier bedrock of the same composition. **(c)** Fragmented thin plated limestone with fractures filled with lateritic material; the bedding is also apparent. **(d)** Gaping fracture in fragmented limestone block; such structures are abundant in the subsurface. In (a) and (b) the location of some significant faults, joints and interfaces is indicated with white lines. All photographs are courtesy of Mr P. Sotiropoulos, Terra-Marine Ltd (http://www.terramarine.gr).

reflectors at the far right of the radargram, between (43 m, 107 ns) and (47 m, 43 ns). The fractures generating Type A reflections may be gaping (as per Fig. 11d) or filled with lateritic material (as per Fig. 11c). The dip of Type B reflections is 10°–20° and is consistent with the dip of the thin-plated limestone bedding and the limestone strata in general, (Fig. 11a, b and c); this is observable at places because the aperture of the interfaces has been widened by damage and weathering and has been filled with lateritic material. Finally, in both Figs. 12 and 13 and at the far left of the radargram one may observe linear reflections dipping up at an angle of −20° to −30°: There are Type C reflections and may correspond to up-dipping primary joints, as indicated in Fig. 11a and b. A similar reflection can be observed at the far right of the section, between (41 m, 85 ns) and (46 m, 42 ns) just in front if the fault mentioned above, while there is clear indication of such features at other parts of the section.

Another way of abstracting and interpreting information will now be discussed. The visual inspection of the data clearly indicates the existence of areas rich in low frequencies; these are quite apparent in the unmigrated section (Fig. 11a) and can also be observed in the migrated section (Fig. 11b). The effect should be a consequence of the properties of the material filling these areas, i.e. preferential absorption of high frequencies in high attenuation domains, and will be investigated in the following.

A synopsis of the spectral content, hence a measure of changes in propagation conditions can be afforded by mapping the frequency of the spectral centroid (or centroid frequency), i.e. the location of the centre of mass of the signal spectrum. This is calculated as a weighted mean of the frequencies present in the signal:

$$f_c = \frac{\int_0^\infty f S(f)\mathrm{d}f}{\int_0^\infty S(f)\mathrm{d}f},$$

where $S(f)$ is the amplitude spectrum. The centroid frequency is expected to decrease (increase) as a function of time, when the signal enters high (low) attenuation domains and is also expected to exhibit consistent gradual downshift in cases of dispersive propagation (e.g. Irving and Knight, 2003). Herein, the calculation of the centroid frequency was performed on the basis of an ultra-high resolution time-frequency representation of the data, (i.e. of the amplitude spectrum at each instant along a trace), computed with the S-transform (Stockwell et al., 1996; also see Irving and Knight, 2003).

Fig. 14a illustrates the centroid frequency (henceforth CF) computed for the migrated section (Fig. 12b). It is straightforward to observe areas where the CF is *significantly* lower than the antenna frequency, and areas where it is significantly higher. At the left half

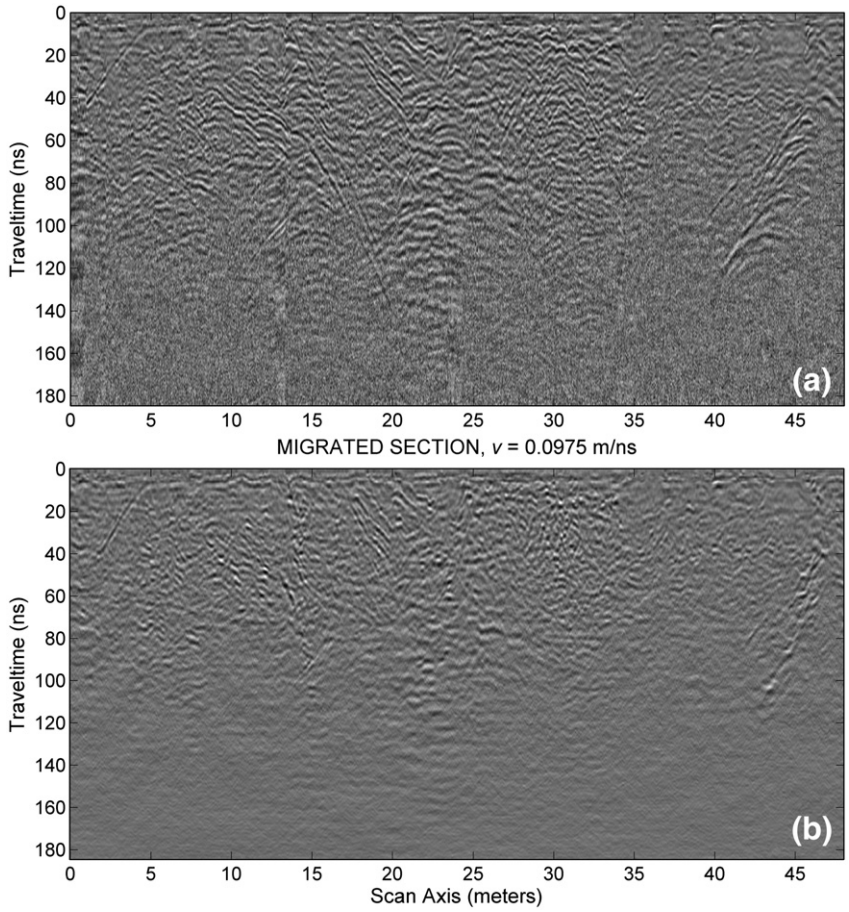

Fig. 12. **(a)** Example radargram obtained at the ridge of Mt. Ktenias, Greece. The data has been pre-processed with time-zero adjustment, global background removal, AGC and elimination of antenna self-clutter (banding). **(b)** The radargram of Fig. 12a after time migration with a velocity of 0.0975 m/ns; the velocity was obtained by direct measurement.

of the section low CFs are generally observed above the 100 ns line and high CFs below it, although pockets of normal (comparable to the antenna frequency) to high CF domains can still be observed above the 100 ns line. At the right half of the section, the low CFs retreat to 60–70 ns. The low CF domain is rather broad between 12 and 28 m and extends to at least 140 ns between 20 and 25 m. An up-dipping low CF area wedging in the high CF domain can also be observed at the far right of the section, collocated with the fault detected in Fig. 13. No gradual shift of the CF is observed, implying that dispersion is not strong. In general, the distribution of the CF indicate the existence of a complex propagation medium in which there are areas of severe high-frequency attenuation and areas of low, or altogether low attenuation from which there are no returns (reflections) and the CF is heavily influenced by the characteristics of random of noise (e.g. below the 100 ns line).

It is possible to use the BSW Filters to isolate the geometry of high or low frequency reflections, hence outline the low or high attenuation domains. Fig. 14b shows the output of a Linear B-Spline/31-Point Hanning Window filter applied over the interval [−80°, 80°] in steps of 10° while tuned at $f \approx 380$ MHz, quite higher than the nominal frequency of the antenna but lower than the CF associated with random noise. Fig. 14c is the same but with the filter tuned at 120 MHz, almost half that of the nominal frequency and approximately centred on the lower frequency end of the spectra that yield the low CF domains. The span of the filter, hence the spectral ratio, was assigned so as to restrain spatial localization (equivalently increase the lateral resolution of extended interfaces). As expected, the results are very different and correspond to reflectors with very different material properties. Thus, Fig. 14b depicts sharp reflections originating at low attenuation interfaces: these are highly localized in time and rich in high frequencies so that they can be observed at short periods (finer temporal scales). Conversely, Fig. 14c depicts broadly localized dull reflections from high attenuation interfaces that absorb high frequencies and enrich the long period content of the signal. This result compares directly with the result of Fig. 10c.

The dull reflectors can be seen to comprise quasi-continuous anastomosing horizons, or to cluster in relatively narrow and vertically extended complexes. Given the geological situation of the study area, the former comprise interfaces between limestone fragments filled with high attenuation material, in which the larger and internally less damaged blocks appear in the form of lenses (hence the anastomoses). The latter (clusters of reflections) are signatures of cavities filled with high attenuation material. Examples of such structures can be observed between 20– 30 m and 20–150 ns, which is the signature of a karstic cavity beneath a bowl-shaped sinkhole, and the up-dipping fault at the far right of the section. In all cases, the dull reflectors are collocated with the low CF domains and the filling material is lateritic in composition.

As mentioned above, at travel times longer than about 100 ns the CF is very high and the radargram is void of any significant reflection. Inasmuch as the signal penetrates to the corresponding depths –dull reflections from the karstic cavity are observed to at least 150 ns — these areas comprise minimally damaged or even healthy rock, in which the bedding and tectonic interfaces have small apertures, are closed and/or dry and do not respond to the wavelengths of the 250 MHz antenna. The fact that the filled cavity extends well into the healthy bedrock is

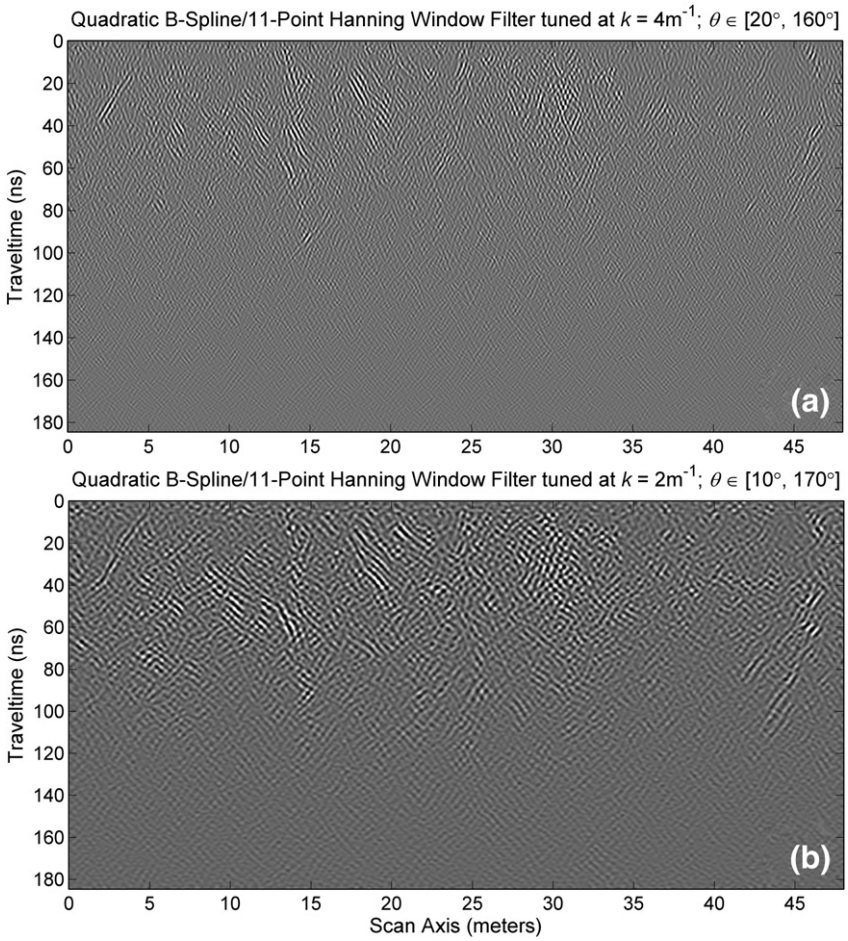

Fig. 13. (a). The data of Fig. 12b after application of a Quadratic B-spline/11-point Hanning Window filter sweeping the arc [20°, 160°] in steps of 10° and tuned at $k \approx 4\ m^{-1}$. **(b)** The data of Fig. 12b after application of a Quadratic B-spline/11-point Hanning Window filter sweeping the arc [10°, 170°] in steps of 10° and tuned at $k \approx 2\ m^{-1}$. The two applications focus on fractures, joints and interfaces with different apertures (of the order of 0.25 m and 0.5 m respectively).

evidence of its tectonic origin, i.e. that it nucleated in a fault or junction of faults. In a final note, typical geological sections with the characteristics described above can be studied in Fig. 11b and 11c.

The Gabor Filter is as effective in extracting the same information. However, because the results are *absolutely comparable* to those of the BSW Filter, corresponding applications will not be presented for the sake of brevity. In conclusion, it is quite clear that the adaptive filtering schemes proposed herein can be focused in many different ways, so as to extract correspondingly different pieces of information at different temporal and spatial scales.

6. BSW Filters or Gabor filters?

As shown (or indicated) above, BSW Filters and Gabor Filters have very comparable performance, quite arguably due to the close relationship of B-Spline wavelets and Gabor functions and the similarities in their design. Nevertheless, the BSW Filter depends on only three parameters (length, span and orientation), whilst the real part Gabor Filter, even following the parameterization of Daugman (1985), depends on five parameters (wavelength, aspect ratio, bandwidth, orientation and phase). Even if the phase is kept constant at zero, the BSW Filter is easier and possibly more intuitive to design. In consequence it may well be a natural first choice.

On the other hand, the half-response bandwidth of the BSW Filter is not adjustable; it is exclusively determined by the choice (order) of the B-Spline wavelet and is marginally affected by the type of the smoothing window. The half-response bandwidth of the Gabor Filter is adjustable and so is the size (breadth) of the spectral lobes (pass bands): it is feasible to design a highly localized Gabor Filter that will be optimally adapted to the data at hand. Thus, whereas in usual conditions it should not make much of a (practical) difference whether to use a BSW or Gabor Filters, there may be demanding circumstances in which the Gabor Filter can be more adaptive and effective than the BSW filter.

Fig. 15a shows a pre-processed 16-bit radargram comprising a 512 samples × 512 traces section with a sampling rate of 0.099 s and a trace spacing of 0.068 m. The data has been collected as part of the Argos survey, with a GSSI SIR-2000 system and 400 MHz antenna. The data is severely contaminated by random noise and the powerful response of several small metallic objects buried just below the surface, which were easy to exhume and identify. Fig. 15b illustrates the output of a 55 × 9 Quadratic B-Spline/Gaussian Window filter, tuned at 400 MHz for $\theta = 0°$. Fig. 15c is the output of a (real part) Gabor Filter with $b = 0.65$, $\gamma = 8$, $\psi = 0°$ and $\lambda = 13$, so as to be tuned at 400 MHz for $\theta = 0°$. Finally, the inset in Fig. 15a shows a typical Fourier spectrum of a trace contaminated by the response of the metallic objects. It comprises a main harmonic at approx. 270 MHz and several higher and lower order harmonics, some of which are indicated in the diagram. The inset in Fig. 15c shows the spectrum of the same trace after application of the BSW filter (continuous line) and Gabor Filter (thick broken line).

In both Fig. 15b and c the noise is effectively removed. However, in the output of the BSW filter, and as also evident in the inset of Fig. 15c, there is still some serious residual contamination in the more severely affected traces. Conversely, the noise is almost completely obliterated by the Gabor Filter, albeit at the expense of some information between 300 and 400 MHz. In fact, the Gabor Filter is more effective at suppressing

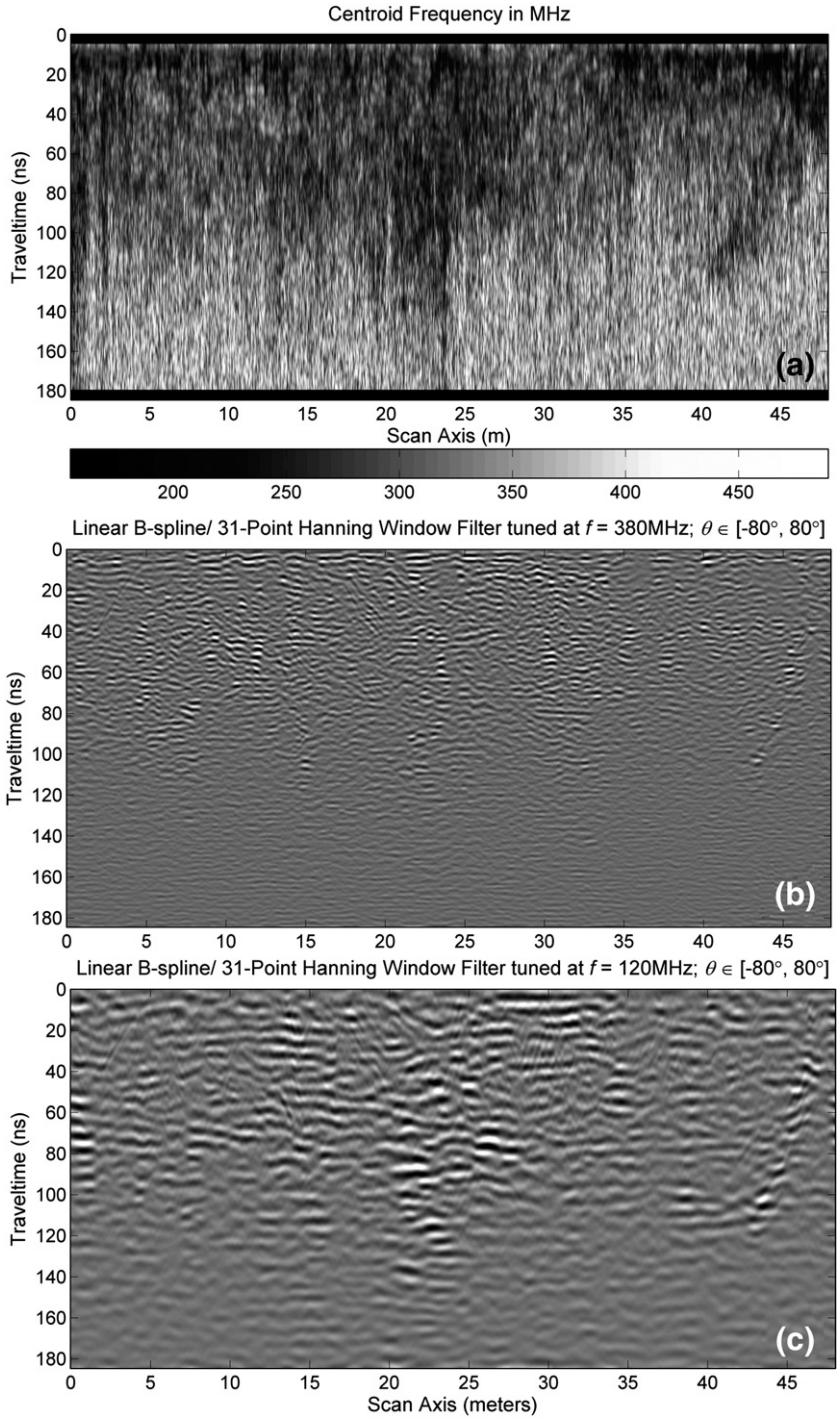

Fig. 14. (**a**). Map of the centroid frequency in MHz, computed from the data of Fig. 12b using the S-transform. (**b**). The data of Fig. 12b after application of a Linear B-Spline/31-Point Hanning Window filter applied over the interval [−80°, 80°] in steps of 10°, while tuned at $f \approx 380$ MHz. This application isolates sharp reflections from low attenuation interfaces: these are rich in high frequencies and can thus be observed at short periods. (**c**) The data of Fig. 12b after application of a Linear B-Spline/31-Point Hanning Window filter applied over the interval [−80°, 80°] in steps of 10°, while tuned at $f \approx 120$ MHz. This application isolates dull reflections from high attenuation interfaces.

the noise than a Cubic BSW filter. The outlines of buried reflective structures are clearly recovered in both Fig. 15b and c; they comprise parts of the floors, the walls and foundations of what was found to be a building with the geometrical characteristics of the temple of Apollo Lyceus as described by Pausanias (confirmation is still pending). However, the tradeoff between complete noise suppression and partial loss of information depends on the specific objectives of the survey and has to be decided by the user.

In a final note, one might ask: in this case, why not apply a sufficiently narrow-band general purpose filter to effectively isolate uncontaminated data? The answer is that the output depends heavily on the second dimension of the filter (span). It is straightforward to demonstrate that any simple $(N \times 1)$ narrow-band filter would not return the same result as per Fig. 15a and b — the residual contamination would still be significant and the loss of information much more severe than any loss of information effected by the BSW and Gabor

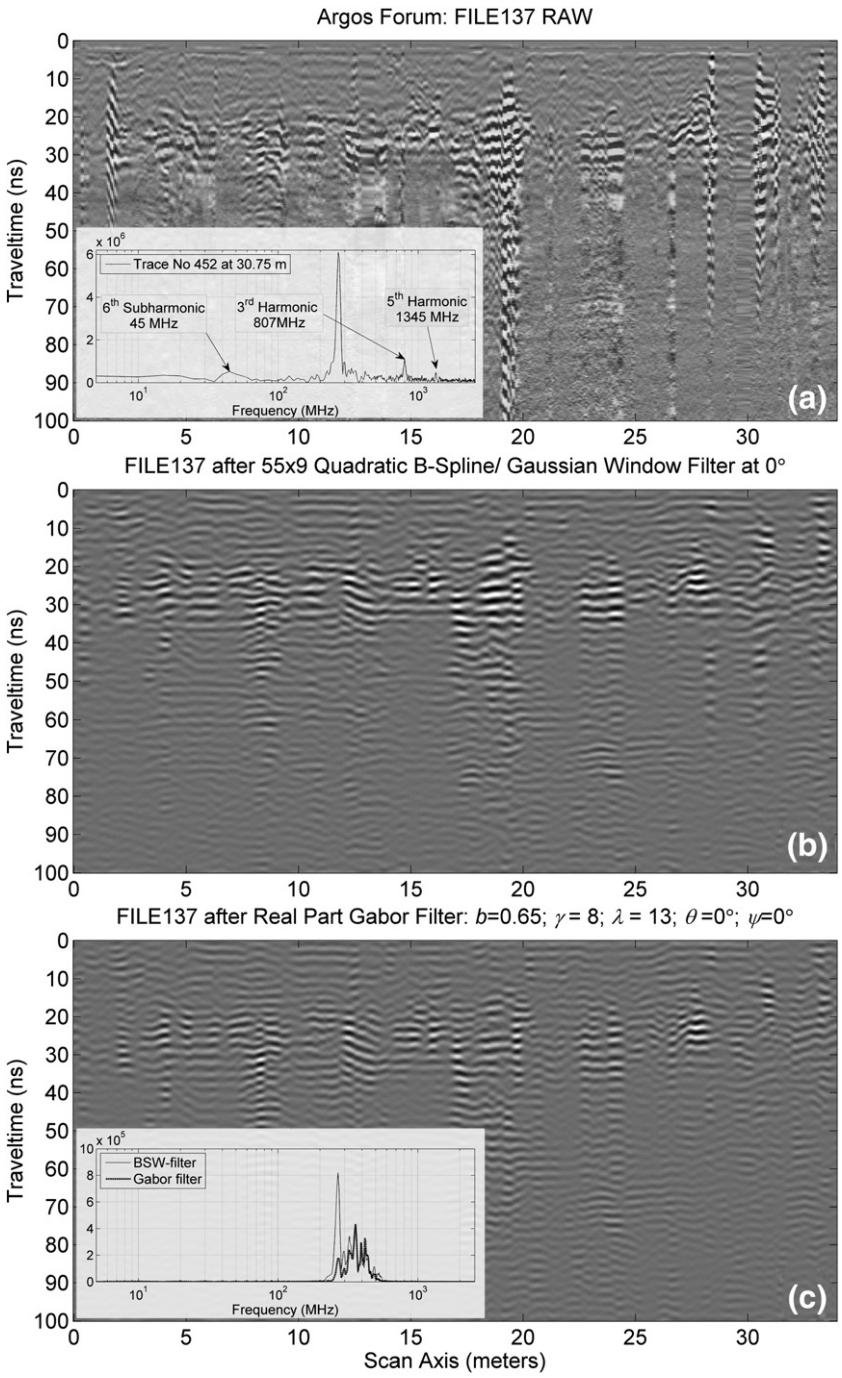

Fig. 15. (a) Pre-processed 16-bit radargram collected with a GSSI SIR-2000 system and 400 MHz antenna; the data is severely contaminated by random noise and the powerful response of several small metallic objects buried just below the surface. The inset figure illustrates the Fourier spectrum of trace 452 at 30.754 m, contaminated by the response of a metallic object; this comprises a fundamental at approx. 270 MHz and several higher and lower order harmonics. **(b)** The same data after application of a 55×9 Quadratic B-Spline/Gaussian Window filter, tuned at 400 MHz (for $\theta=0°$). **(c)** The same data after application of a (real part) Gabor filter with $b=0.65$, $\gamma=8$, $\psi=0°$ and $\lambda=13$, tuned at 400 MHz (for $\theta=0°$). The inset figure illustrates the spectrum of trace 452 after application of the BSW filter (continuous line) and the Gabor filter (thick broken line).

Filters. Such examples will not be given, however, for the sake of brevity.

7. Epilogue

The present work introduces a directional filtering technique based on the (continuous) wavelet transform and designed to facilitate the study of geometrical information in two-dimensional (B-scan) GPR data. Albeit computationally intensive, the technique is simple to use and very powerful: with a little trial and error the analyst may isolate/extract information about any resolvable structural scale at any resolvable frequency or wavenumber (temporal or spatial scale).

The filters studied herein comprise (a) one-dimensional B-Spline Wavelets, (b) two-dimensional arrays of parallel B-Spline Wavelets (longitudinal direction) tapered by a window function in the transverse direction and, (c) two-dimensional Gabor Filters. These may produce scale-and-dip-specific representations of the input

GPR-data as they can be rotated to any desired orientation and applied under adaptive control, so as to focus (tune) at specific frequencies or wavenumbers. Furthermore, it is shown that the same-scale and dip-specific representations obtained at different orientations may be combined in the least-squares sense to reconstruct dip-independent representations of the data at specific temporal or spatial scales (frequencies or wavenumbers). Both types of filter perform comparably, although Gabor Filters appears to be more adaptive in some extreme cases than BSW Filters. Conversely, the latter are quite simpler to design and experiment with, as they depend on only three parameters (length, span and orientation).

The proposed filtering method can be used to:

a) Enhance the S/N ratio in a manner particularly suitable for GPR data, because the frequency response of the filters, especially that of the B-Spline wavelets, mimics the frequency characteristics of the source wavelet.
b) Isolate/enhance geometrical information for further scrutiny.
c) Exploit the temporal localization characteristics of the filter outputs to investigate the characteristics of signal propagation (hence material properties), albeit indirectly. This is possible because signal attenuation and temporal localization are closely associated. Thus, interfaces in low attenuation domains will tend to produce sharp reflections rich in high frequencies and fine-scale localization as a function of time. Conversely, interfaces in high attenuation domains will tend to produce dull reflections rich in low frequencies and broad localization.

The technique has its caveats! For instance, caution is required when the rotation angle approaches $n\pi/2$ with n integer: Frequency-tuning breaks down when n is odd and wavenumber-tuning breaks down when n is even. In both cases this happens because the length or wavelength of the filter becomes prohibitively short. Although there are remedies, e.g. to resample the data at higher temporal or spatial rates, there are still limits beyond which tuning is no longer practical. On the other hand it should be reasserted that this limitation does not have serious practical consequences. In the first case (frequency-tuning) and at dip angles of the order of $(2n+1)\pi/2$, the arrivals are reflected from (sub) vertical interfaces and propagate (sub)horizontally. Essentially, they comprise spatial features dependent on the wavenumber and may, therefore, be processed with wavenumber-tuneable filters. Likewise, in the case wavenumber-tuning and at dip angles of the order of $n\pi$, the arrivals are reflected from (sub)horizontal interfaces and propagate (sub)vertically; they are essentially temporal features dependent on the frequency and can be processed with frequency-tuneable filters.

A final question would be of whether other techniques exist, capable of the same results. The answer is affirmative. For instance there may be cases where conventional f–k filters will perform equally well with the proposed filtering scheme, or even better. However, with increasing structural and/or noise complexity, such filters may be very difficult to design. The advanced orientation-sensitive X-let transforms may also offer efficient alternatives — their merits and limitations have already been briefly discussed in Section 1 (Introduction). Inasmuch as they will be the subject of follow-up research, they will not be elaborated herein. At any rate, none of the alternative methods is as simple and intuitive as the filtering scheme proposed herein.

In a final note, it should be mentioned that a MATLAB™ implementation of the proposed filtering scheme (complete with a detailed user's manual) is freely available as part of an updated distribution (Release 3) of the matGPR software (Tzanis, 2010).

References

Brinks, R., 2008. On the convergence of derivatives of B-splines to derivatives of the Gaussian function. Computational and Applied Mathematics 27 (1), 79–92.

Candès, E., 1999. Harmonic analysis of neural networks. Applied and Computational Harmonic Analysis 6, 197–218.

Candès, E., Donoho, D., 1999. Ridgelets: A key to higher-dimensional intermittency? The Royal Society of London. Philosophical Transactions. Series A. Mathematical, Physical and Engineering Sciences 357, 2495–2509.

Candès, E., Donoho, D., 2003a. Continuous curvelet transform: I. Resolution of the wavefront set. Applied and Computational Harmonic Analysis 19, 162–197.

Candès, E., Donoho, D., 2003b. Continuous curvelet transform: II. Discretization and frames. Applied and Computational Harmonic Analysis 19, 198–222.

Canny, J., 1986. A computational approach to edge detection. IEEE Transactions on Pattern Analysis and Machine Intelligence 8 (6), 679–698.

Chui, C.K., 1992. An Introduction to Wavelets. Academic Press, New York.

Daubechies, I., 1992. Ten Lectures on Wavelets. CBMS Regional Conference Series in Applied Mathematics. SIAM, Philadelphia, PA, USA.

Daugman, J.G., 1985. Uncertainty relations for resolution in space, spatial frequency, and orientation optimized by two-dimensional visual cortical filters. Journal of the Optical Society of America 2, 1160–1169.

Deighan, A.J., Watts, D.R., 1997. Ground-roll suppression using the wavelet transform. Geophysics 62, 1896–1903.

Demanet, L., Ying, L., 2007. Wave Atoms and Sparsity of Oscillatory Patterns. Applied and Computational Harmonic Analysis 23 (3), 368–387.

Do, M., Vetterli, M., 2005. The contourlet transform: an efficient directional multiresolution image representation. IEEE Transactions on Image Processing 14 (12), 2091–2106.

Donoho, D., 1999. Wedgelets: nearly minimax estimation of edges. Annals of Statistics 27 (3), 859–897.

Donoho, D., Huo, X., 2002. Beamlets and multiscale image analysis. In: Barth, T., et al. (Ed.), Multiscale and Multiresolution Methods: Springer Lecture Notes in Comput. Sci. Eng., vol. 20, pp. 149–196.

Feichtinger, H.G., Strohmer, T., 1998. Gabor Analysis and Algorithms. Birkhäuser0817639594.

Feichtinger, H.G., Strohmer, T., 2003. Advances in Gabor Analysis. Birkhäuser0817642390.

Freeman, W., Adelson, E., 1991. The design and use of steerable filters. IEEE. Transactions on Pattern Analysis and Machine Intelligence 13 (9), 891–906.

Grigorescu, C.E., Petkov, N., Kruizinga, P., 2002. Comparison of texture features based on Gabor filters. IEEE Transactions on Image Processing 11 (10), 1160–1167.

Grigorescu, C., Petkov, N., Westenberg, M.A., 2003. Contour detection based on nonclassical receptive field inhibition. IEEE Transactions on Image Processing 12 (7), 729–739.

Irving, J.D., Knight, R.J., 2003. Removal of wavelet dispersion from ground-penetrating radar data. Geophysics 68 (3), 960–970.

Jeng, Yih, Lin, C.-H., Li, Y.-W., Chen, C.-S., Huang, H.-H., 2009. Application of multiresolution analysis in removing ground-penetrating radar noise. Frontiers+Innovation — 2009 CSPG-CSEG-CWLS Convention, pp. 416–419.

Katunin, A., Korczak, A., 2009. The possibility of application of B-spline family wavelets in the diagnostic signal processing. Acta Mechanica et Automatica 3 (4), 43–48.

Kruizinga, P., Petkov, N., 1999. Non-linear operator for oriented texture. IEEE Transactions on Image Processing 8 (10), 1395–1407.

Leblanc, G.E., Morris, W.A., Robinson, B., 1998. Wavelet analysis approach to de-noising of magnetic data. SEG Expanded Abstract, pp. 554–557.

Lee, T., 2008. Image representation using 2D Gabor wavelets. IEEE. Transactions on Pattern Analysis and Machine Intelligence 18 (10), 1–13.

Little, S.A., 1994. Wavelet Analysis of Seafloor Bathymetry: An Example. In: Foufoula-Georgiou, E., Kumar, P. (Eds.), Wavelets in Geophysics. Academic Press, San Diego, pp. 167–182.

Little, S.A., Carter, P.H., Smith, D.K., 1993. Wavelet analysis of a bathymetric profile reveals anomalous crust. Geophysical Research Letters 20 (18), 1915–1918.

Lu, Y., Do, M., 2007. Multidimensional directional filter banks and surfacelets. IEEE Transactions on Image Processing 16 (4), 918–931.

Lucius, J.E., Powers, M.H., 2002. GPR Data Processing Computer Software for the PC. USGS Open-File Report 02–166.

Mallat, S.G., 1999. A Wavelet Tour of Signal Processing. Academic Press.

Mallat, S., Peyré, G., 2007. A review of bandlet methods for geometrical image representation, Numer. Numerical Algorithms 44 (3), 205–234.

Matos, M.D., Osorio, P.M., 2002. Wavelet transform filtering in the 1D and 2D for ground roll suppression. SEG Expanded Abstract, pp. 2245–2248.

Miao, X., Cheadle, S.P., 1998. Noise attenuation with wavelet transforms. SEG Expanded Abstract, pp. 1072–1075.

Mohideen, S.K., Perumal, S.A., Sathik, M.M., 2008. Image de-noising using discrete wavelet transform. International Journal of Computer Science and Network Security, 8, pp. 213–216 (January).

Nuzzo, L., Quarta, T., 2004. Improvement in GPR coherent noise attenuation using τ–p and wavelet transforms. Geophysics 69, 789–802.

Simoncelli, E., Freeman, W., Adelson, E., Heeger, D., 1992. Shiftable multiscale transforms. IEEE Transactions on Information Theory 38 (2), 587–607.

Stockwell, R.G., Manshinha, L., Lowe, R.P., 1996. Localization of the complex spectrum: The S-transform. IEEE Transactions on Signal Processing 44, 998–1001.

Stollnitz, E.J., DeRose, T.D., Salesin, D.H., 1995. Wavelets for computer graphics: a primer, Part 1. IEEE Computer Graphics and Applications 15, 76–84 (May).

Tzanis, A., 2010. matGPR Release 2: a freeware MATLAB® package for the analysis & interpretation of common and single offset GPR data. FastTimes 15 (1), 17–43.

Ueda, M., Lodha, S., 1995. Wavelets: An Elementary Introduction and Examples. University of California, Santa Cruz: Technical Report UCSC-CRL-94-47.

Unser, M., 1992. On the asymptotic convergence of B-splίne wavelets to Gabor functions. IEEE Transactions on Information Theory 38 (2), 864–872.

Unser, M., 1997. Ten good reasons for using spline wavelets. Proc. SPIE: Wavelets Applications in Signal and Image Processing V, vol. 3169, pp. 422–431.